UNIVERSITY OF CALIFORNIA
RIVERSIDE

Manipulation of Laser-Induced Cavitation Bubbles for Microfluidic and Micro-Targeting Applications

A Dissertation submitted in partial satisfaction
of the requirements for the degree of

Doctor of Philosophy

in

Mechanical Engineering

by

Vicente Robles

September 2022

Dissertation Committee:
Dr. Guillermo Aguilar, Co-Chairperson
Dr. Natanael Cuando Espitia, Co-Chairperson
Dr. Masaru P. Rao

The Dissertation of Vicente Robles is approved:

_____

_____

_____

Committee Chairperson

University of California, Riverside

ACKNOWLEDGEMENTS

I would like to thank my advisor, Dr. Guillermo Aguilar for his guidance during my graduate studies. He opened an opportunity for me to join his lab as an undergraduate student and challenged me throughout the years as I continued as a masters and Ph.D. student. Dr. Natanael Cuando-Espitia has also provided ample support and mentorship as co-advisor, especially during my final transitions at UCR. I would also like to thank my committee member, Dr. Masaru P. Rao, for guidance in the advancement of my work.

Apart from my committee, I learned a tremendous amount of technical knowledge from collaborations with several friends, students, and researchers: Dr. Darren Banks, Dr. Luis F. Devia-Cruz, Dr. Bin Zhang, Dr. Elias H. Penilla, Dr. Enoch Gutierrez-Herrera, Dr. Noe Zamora-Romero, Dr. Mildred S. Cano-Velazquez, Dr. Santiago Camacho-Lopez, Dr. Juan Hernandez-Cordero, Dr. David L. Halaney, and Mr. Juan Carlos Gonzalez-Parra. I would also like to thank the many additional colleagues and friends whom I crossed paths with and shared positive experiences with while at UCR: Mr. Jay Zarekar, Mr. Kendrick Rady, Dr. Nami Davoodzaeh, Dr. Kendrick Mensink, Mr. Yair Sanchez, Dr. Rosalinda Lopez, Miss Crysthal Alvarez, and Mr. Ismael Martinez.

Thank you to the UCR Graduate Division for continued support starting from my first year in graduate school through my last. Without financial support from the Eugene Cota Robles Fellowship and the Ford Foundation Predoctoral Fellowship, pursuing my Ph.D. would have been much more difficult.

In addition, mentorship and guidance from several people and groups have been invaluable during my journey towards higher education. Thank you to my high school

teachers and counselor who have always remained sources of support, to the Nicholas Academic Center family who helped propel me into college. Thank you to Dr. Tony Jimenez, to the professors from the Pomona College Physics and Astronomy Department, to the SROP and MSRIP programs, and to and Maria Franco-Gallardo for their mentorship and support.

The text of this dissertation, in part, is a reprint of the material as it appears in the Journal, Physics of Fluids, 2020, “Soft Material Perforation via Double-Bubble Laser-Induced Cavitation Microjets”.

DEDICATION

I dedicate this to my family. To my father Vicente, my mother Gloria, my sisters Cynthia and Cristina, my wife Tyler and my extended family. They all provided never ending love and encouragement and were always present during the toughest of times. Also to my furry friends who can't read this, but never fail to make me smile: Tyson, Brandon, and Titan.

ABSTRACT OF THE DISSERTATION

Manipulation of Laser-Induced Cavitation Bubbles
for Microfluidic and Micro-Targeting Applications

by

Vicente Robles

Doctor of Philosophy, Graduate Program in Mechanical Engineering
University of California, Riverside, September 2022
Dr. Guillermo Aguilar, Co-Chairperson
Dr. Natanael Cuando Espitia, Co-Chairperson

Cavitation is a micron-scale process in which short-lived vapor bubbles form and collapse, giving way to intense, localized effects in the surrounding liquid. The phenomenon of cavitation was first noted to cause undesired damage on nautical equipment via erosion from strong emitted shockwaves as well as microjets that form when cavitation collapses near solid boundaries. More recently, cavitation studies have sought to exploit this process as a multitool for applications such as photothermal therapy, microfluidic pumping, and surface cleaning among other uses. However, several cavitation mechanisms continue to contribute to mechanical failure via surface erosion, thermal damage and collateral impacts expanding beyond the intended targeted regions. While fluid and optical properties may influence the formation threshold of cavitation, the physical surroundings such as interfaces and boundaries largely determine the collapse dynamics which is the primary effect utilized for said applications. An overwhelming number of investigated

applications use a single cavitation event near a static structure to initiate jet formation, but this limits the available control to the stand-off distance defined by the ratio between the bubble distance to the wall and the maximum bubble radius. Two studies are presented which demonstrate how laser-induced cavitation impact can be controlled effectively or avoided entirely.

First, a detailed study investigates how varying the temporal and spatial separation of two interacting cavitation bubbles can affect the resulting jet speed. The double bubble system is found to generate fast jets capable of perforating soft materials with a minimized surface damage compared to a single bubble impact. A novel experimental proof of concept is reported to use this system for needless injection without the need for clean room fabrication of micronozzles as is required by previous works. A second experimental study reports the use of simple casted gas entrapping microstructures to influence the migration of cavitation collapse. The air pockets act as compressible interfaces and expand during the primary cavitation event and repel the bubble away from the surface. This process can be employed as a method to mitigate cavitation erosion or enhance agitation in low Reynolds number flows in an on-demand and localized manner. The final section briefly explores characterization of thermocavitation, a second form of cavitation formation via energy deposition by continuous wave irradiation.

Contents

List of Figures

List of Tables

List of Symbols

Symbol	Definition	Typical Units
γ	Stand-off distance	----
τ	Bubble-bubble phase	----
γ_{BB}	Bubble-bubble stand-off	----
γ_{BT}	Bubble-target stand-off	----
L_P	Penetration length	µm
D_R	Damage radius	µm
P_{Jet}	Jet pressure	Pa
ϵ_{energy}	Injection efficiency	----
W_r	Wetted region	----
β	Microstructure pitch	µm
λ	Wavelength	nm

Chapter 1. Introduction

A crab living peacefully in Deep Ocean, wakes up for a morning walk, when suddenly, *BANG!* It gets struck and is becomes the mantis shrimp's breakfast. The mantis shrimp holds the record for the fastest punch in the animal kingdom due to its naturally engineered load-and-release appendage strike. The punch velocity is so fast that it causes water to quickly vaporize and form a vapor bubble. As the bubble collapses immediately after the appendage striking, it releases an intense shockwave killing prey almost instantly. This effect is called cavitation.

Cavitation, in its simplest definition, is the formation of a vapor bubble in a fluid followed by its collapse and the emission of a high-pressure shockwave. This phenomenon is present in environments outside of the mantis shrimp punch (and the pistol shrimp clamp) and has been a problem for engineers in various fields, causing significant material breakdown, erosion, vibrations, noise pollution other unfavorable outcomes. The word "cavitation" was coined in 1895 by naval architecture R. E. Froude when he sought to study the source of damage on hydraulic turbines, pumps and blades. Shortly after in 1917, Rayleigh began investigating the dynamics that cause cavitation to form and the consequences that follow. Early researchers reported that the bubbles were formed due to low pressure regions which occurred in high velocity areas.

Cavitation can be formed under tension (hydrodynamic and acoustic cavitation) when a rapid decrease in pressure causes the small volume of liquid to drop past the saturation vapor pressure and transform from a liquid state to a gaseous state. During this process, the liquid temperature can be considered constant. Acoustic cavitation, like

hydrodynamic cavitation, is produced by pressure differentiations present in fluid flow. This change in pressure arises due to incident sound waves in the ultrasound frequency range of 22 kHz to 1 MHz A cloud of microscopic gas bubbles results from the conversion of kinetic energy from vibrations to the heating of the liquid. The bubbles quickly grow during rarefaction half-cycles of the applied longitudinal wave. This growth is due a term known as rectified diffusion which is mass transfer in the form of gas into the bubble. When the bubbles reach a critical diameter, they quickly collapse. Often, there is sonoluminescence, an emission of energy in the form of photons during the collapsing phase. Cavitation can also be formed by dielectric breakdown by applying a high voltage between two electrodes submerged in water.

1.1. **Formation of Optical Cavitation**

The works in the following chapters focus on another formation of cavitation via energy deposition by a laser (optical cavitation) which allows precise formation of bubbles in time and space. Optical cavitation can be initiated in two processes depending on the type of laser used: continuous-wave or pulsed-wave laser. Most of the work presented here is conducted using pulse-wave lasers and is referred to as “laser-induced cavitation”. Continuous-wave laser-initiated cavitation is referred to as “thermocavitation” and will be briefly describe in Chapter 4 along with results on the topic of its characterization.

Laser-induced cavitation occurs when short laser pulse exposures in the range of micro-femtosecond are tightly focused into a liquid medium and lead to optical breakdown. Optical breakdown occurs through a process known as cascade or avalanche ionization

where an initial minor number of seed electrons are excited during laser irradiation and a buildup of additional electrons reach a density of 10^{18} electrons / cm^3. The seed electrons are present from pre-existing impurities in the liquid which aid in lowering the breakdown threshold. When the photons are irradiated, the seed electrons absorb the optical energy and collide with particles such as molecules and ions and in return free additional electrons. This process is repeated multiple times as the energy absorbed exceeds the ionization potential. When the critical electron density is reached, a plasma is formed which reaches temperatures in the orders of 10^4 Kelvin and pressures of 10^4 - 10^5 Pa. The extreme pressures and temperatures are limited to the plasma volume which typically reaches diameters of ~100 μm. The plasma is short lived and undergoes a rapid radial thermal expansion at supersonic speeds, emitting a compressive shockwave. The shockwave travels radially outward and slows to a pressure wave at the speed of sound, gradually losing energy. As the plasma expands, it cools and decays through electron-ion recombination producing a visible flash. At the same time, the surrounding parcel of fluid is vaporized, and a vapor bubble is formed. The process of cascade breakdown is probabilistic as it depends on seed electrons being present in the volume irradiated during laser excitation. Thus, a probability of breakdown or cavitation formation is typically given to describe the degree of laser fluence used in experiments.

The high internal pressures cause the bubble walls to expand until the enlarged volume allows the internal pressure to decrease. As the bubble grows, the vapors are partially condensed through the bubble wall which causes the growth to slow. Then, the internal pressures reach the vapor saturation pressure which is smaller than the surrounding

hydrostatic and atmospheric pressures and the bubble begins to collapse. As the bubble collapses, the internal components are compressed, and the pressure again begins to increase. If the gases are compressed enough, they increase in temperature and lead to a re-expansion of a bubble. Multiple rebounds of growth and collapse may be observed if enough energy is stored in the primary bubble which is determined by the optical energy input. Finally, as the energy is diminished, residual bubbles of dissolved gas persist in the breakdown region for a limited time.

When a cavitation event is formed in the presence of a solid boundary, the bubble wall furthest from the wall experiences a faster inflow during the collapse. This causes an asymmetrical collapse in a toroidal-shape in which the bubble pierces itself and forms a microjet that moves towards the boundary surface. Upon impact, the liquid jet creates ring vortices that expand radially outward from the site of impact. If the jet impact pressure surpasses the boundary's yield strength, pitting occurs. This liquid jet formation has been used in various applications particularly in the biomedical field to target kidney stones, cancel cells, and even for transfusion of cells among other examples. However, the strength of the liquid jet formation depends on the standoff distance, γ, which is a dimensionless parameter defined by the distance of the bubble center to the wall divided by the maximum radius reached by the bubble.

In the next chapter the interaction of two cavitation bubbles is explored as a method to generate fast microjets without requiring a nearby solid boundary. Chapter 3 explores the use of entrapped air pockets in PMDS microstructures to influence the migration of a cavitation event away from a surface. As will be detailed, this technique may assist in

reducing cavitation erosion, or may be used as an agitation source in microfluidics where laminar flow is prevalent Chapter 4 briefly describes cavitation formation via continuous-wave lasers and discusses the similarities and differences to pulsed-wave cavitation. Finally, Chapter 5 summarizes the findings of this work and gives a brief outlook on future avenues of study.

Chapter 2. Soft Material Perforation Via Double-Bubble Laser-Induced Cavitation Microjets

V. Robles[1], E. Gutierrez-Herrera[1,2], L. F. Devia-Cruz[3], D. Banks[4], S. Camacho-Lopez[3], and G. Aguilar[1]*

[1] *Department of Mechanical Engineering, University of California, Riverside, Riverside, 92521, California, USA,*
[2] *Instituto de Ciencias Aplicadas y Tecnología, Universidad Nacional Autónoma de México, Ciudad de México 04510, México.*
[3] *Centro de Investigación Científica y de Educación Superior de Ensenada, Departamento de Óptica, Carretera Ensenada – Tijuana 3918, Zona Playitas, Ensenada, B.C., C.P. 22860, México*
[4] *Department of Mechanical Engineering, California State University Fullerton, Fullerton, CA, USA 92831*
**Corresponding author: gaguilar@engr.ucr.edu*

Abstract

The resulting jet of two interacting laser-induced cavitation bubbles is optimized and studied as a technique for micro-scale targeting of soft materials. High controllability of double-bubble microjets can make such configuration favorable over single bubbles for applications where risk of ablation or thermal damage should be minimized such as in soft biological structures. In this study double-bubble jets are directed towards an agar gel-based skin phantom to explore the application of micro-scale injection and towards a soft paraffin to quantify targeting effectiveness of double-bubble over single-bubble jetting. The sharp elongation during the double-bubble process leads to fast, focused jets reaching average magnitudes of $U_{jet} = 87.6 \pm 9.9\, m/s$. When directed to agar, the penetration length and injected volume increase at approximately 250 μm and 5 nL per subsequent

jets. Such values are achieved without the use of fabricated micro nozzles seen in existing needle-free laser injection systems. In soft paraffin, double-bubble jetting produces the same penetration length as single-bubble jetting, but with approximately a 45% reduction in damage area at a 3x greater target distance. Thus, double-bubble jetting can achieve smaller impact areas and greater target distances, potentially reducing collateral thermal damage and effects of strong shockwave pressures.

2.1. Introduction

Cavitation bubbles are relatively small and short-lived (micron spatial and microsecond temporal scales), but produce strong, localized mechanical, optical, chemical and thermal changes, making them prime candidates for micro targeting applications such as surface cleaning [1–3], cell targeting [4–8], and potential enhancement of localized heat transfer [9,10], among others. Specifically, cavitation has been exploited for the asymmetrical collapse that occurs in the vicinity of a boundary and forms a jet towards the target [11–14]. As will be explained in Section 2.3, the resulting jet magnitude depends on the dimensionless stand-off distance (γ) determined by 1) the bubble's maximum radius, and 2) the distance between the bubble initiation and the boundary (i.e. target distance). The former can be controlled by changing the focal spot size or varying the laser fluence by an attenuator, both of which can be experimentally restricting. Thus, the target distance is the single parameter that can feasibly control the jet speed in a wide range. However, close bubble-boundary proximities can result in unpredictable fast jets, unintended ablation, and exposure to high plasma temperatures and shockwave pressures

(i.e. 6000-15,000 K and 2-6 GPa [15–17]) which lead to undesirable damage of the target surface. Lechner *et al*. computationally reported, that at close proximities ($\gamma \leq 0.2$), resulting jet speeds may surpass the field's previously accepted magnitude of ~100 m/s by reaching ~ 2000 m/s [18]. Additionally, Dijkink *et al.*, used cavitation shear forces to perforate cells for molecular intake; however at small γ, the cells central to the jet impingement region experienced decreased viability, likely due to thermal damage or detachment from intense pressures[4]. Furthermore, the jetting behavior of a bubble near a boundary is influenced by the surface properties. Particularly in the field of medical laser applications, some researchers describe complex bubble dynamics while observing the interaction and behavior of cavitation bubbles near elastic boundaries (emulating mechanical properties of tissue) [19–23]. Thus, it is essential for many applications to effectively increase γ thereby minimizing detrimental effects, while maintaining the required range of jet speeds for the application of interest and removing strong dependence on a present target and its properties. A technique to generate jets without the need of a boundary or fabricated device is to utilize two neighboring cavitation bubbles [24–26]. Thus, the interaction of two bubbles may provide a unique method to increase γ and enhance the controllability of fast jets to open viable avenues for applications of tissue cutting, lithotripsy and needle injection alternatives.

Traditionally, needle injections have been proven effective; however, sources of contamination, large volumes of medical wastes among phobias have driven the search for alternatives such as piezoelectric actuator-driven jets [27], spring driven jet injectors [28] and laser-based systems [29–33], the latter having gained attention for greater controllability.

Laser-based injection systems principally operate with jets formed by displacing a liquid through a micronozzle[34] with the growth of a thermocavitation bubble. However, the requirement of tapered micronozzles and channels call for complex fabrication and are prone to clogging, thus reducing reproducibility. Continuous wave laser methods [30,35,36], typically use a corrosive copper nitrate solution because the incident wavelength should be strongly absorbed to initiate thermocavitation; -a thermal process in which an explosive phase transition occurs [9,37,38]. In this case, the liquid faces relatively long heating stages (i.e. tens of milliseconds) which may chemically change and deem the drug ineffective. Methods to tackle this issue have been proposed by separating the cavitating liquid from the drug with a flexible membrane [39], but the device's fabrication is further complicated. Additionally, thermocavitation occurs quasi-periodically, with random jitter in bubble initiation times and bubble sizes at low powers [37], making the volume of injection only partially predictable. Thus, pulsed laser-induced bubbles remain superior for controllability and their capability to be generated in transparent media with short lived, minimal heating (<1.3 ms, and < 12.8 °C [40]). To the best of our knowledge, the possible effectiveness of using double-bubble jetting for needle-free injection has not been explored. Neighboring cavitation bubbles generated by pulsed lasers may allow for fast jets to be initiated without the need for fabricated nozzles or relying on absorbing solutions and with minimal localized heating.

In the presented work, we analyze the effects of spatial and temporal separations of double-bubble configurations, on the resultant jet speed. At optimized parameters, we direct fast jets towards soft materials to show the potential of double-bubble arrangements

to replace single-bubble jetting in applications of micro-targeting. Single- and double-bubble arrangements are compared by characterization of the damage sites (penetration lengths and areas) resulting from the two processes. Furthermore, the possible application of double-bubble configurations for needle-free injections is considered by exploring the formation of cavities in agar-gel phantoms.

2.2. Materials and Methods

2.2.1. Bubble Generation and Imaging of Jet Dynamics

Two 1 mm diameter sized bubbles were generated in deionized (DI) water using two Q-switched Nd: YAG lasers (EKSPLA NT 342, Vilnius, Lithuania and Continuum Surelite SLII-10, California, USA) with 1064 nm wavelengths, and 6 ns pulse duration. As shown in Figure 1, the beams were individually collimated and focused antiparallel with matching aspheric lenses (f = 11 mm) into a glass cuvette containing DI water. The X-axis alignment provided the highest temporal resolution for analyzing the jet dynamics. Each laser's energy was individually adjusted with an attenuator composed of a half wave plate (1/2 WP) and polarizing beam splitter (PBS) such that the bubbles were of similar size regardless of miniscule differences between beam profiles. The experiments were conducted with approximately 1 mJ energies. The energies were measured following sets of experiments before the cavitating lenses (f_1 and f_2) using a Gentec-EO energy meter (QE25LP-S-MB-QED-D0, Oregon, USA).

The bubble interaction and jetting dynamics were studied using high speed (HS) shadowgraphy at 193,771 frames per second (fps) and 48 x 256-pixel resolution using a HS Phantom camera (Miro M310, USA) coupled with a long-distance Infinity microscope (KC VideoMax, IF-3 Objective, USA). The imaging resolution (~22 µm per pixel) averaged over the elapsed time per frame accounts for an uncertainty in average velocity measurements of 2.1 m/s. The events were back-illuminated with a diffuse white light source. The camera resolution was reduced to 64 x 48-pixels to accurately measure a single bubble's expansion time at an enhanced rate of 3.8 x 10^5 fps. A Berkeley Nucleonics pulse delay generator (PDG) (M-555, California, USA) was used to externally synchronize and trigger both lasers and HS camera up to a 1 ns resolution (refer to Figure 1).

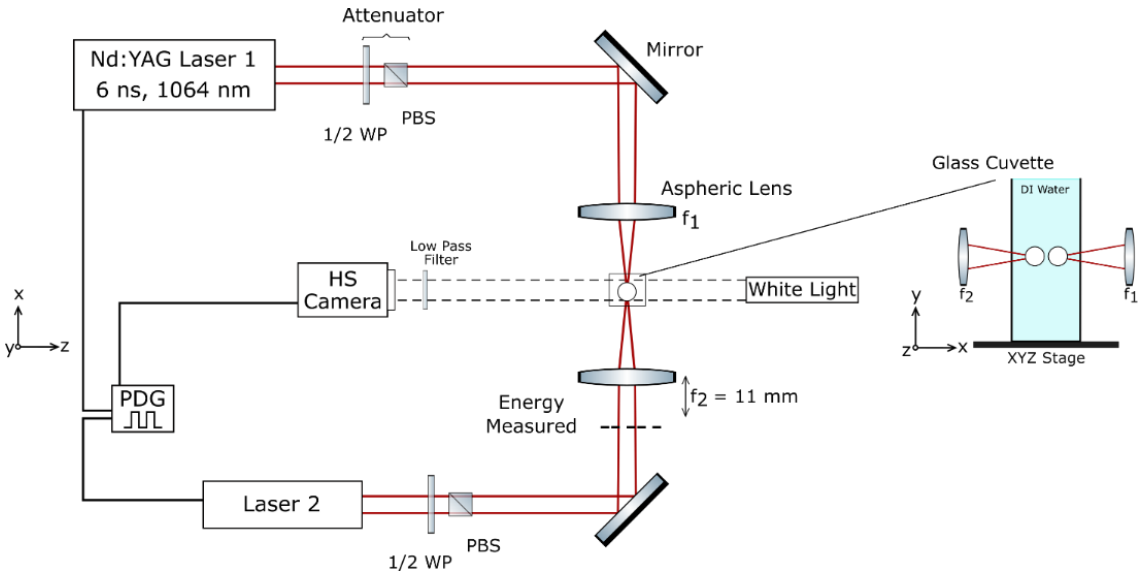

Figure 2-1: A schematic of the experimental setup. Laser 1, Laser 2 and the high speed (HS) Camera are synchronized and activated with the pulse delay generator (PDG). Laser 1 and Laser 2 energies are controlled by attenuators. Inset depicts lateral view of the cuvette setup used for imaging of jetting dynamics.

2.2.2. Target Preparation

Two target materials were used to 1) characterize and compare the damages from single-bubble jetting (SBJ) and double-bubble jetting (DBJ), and 2) explore DBJ as a proof of concept for needle-free injection. First, a soft paraffin (i.e. Petroleum Jelly, Vaseline) was used for its hydrophobicity and malleability, allowing to characterize the damage areas and penetration lengths of jet impingement. Approximately 150 mg of soft paraffin was applied onto 1 x 2 cm glass substrates and slowly heated to 60 ˚C until the soft paraffin liquified and became transparent. The samples were cooled to room temperature and solidified on the glass as smooth 500 μm thick layers. Once solid, the samples became semi-opaque, preventing real time lateral view of the impingement process. Additionally, the soft paraffin's semisolid viscous properties could not accurately portray the material properties of soft tissue for applications of injection. Thus, an optically transparent agar gel was used as a tissue phantom model for its comparable mechanical properties (Young's modulus) to tissue. A concentration of 1% agar was chosen as it provides a Young's Modulus of $E \sim 20$ kPa [41], comparable to the lower limit of skin's modulus [42]. The agar samples were prepared with 1:100 ratio of Molecular Genetics agar powder (BP1423, Mexico) to DI water by weight. The mixture was continuously mixed and heated to 90 ˚C until the powder was dissolved, and no granules were observed. The solution was then poured into open-ended cuvettes and cooled to 4 ˚C, solidifying into smooth 1 cm^2 rectangular prisms.

2.3. Double-Bubble Jetting Parameters

Figure 2 shows a depiction of two subsequent neighboring cavitation bubbles resulting in the formation of a slow bulk motion countered in the opposite direction by a thin high-speed jet. As the second initiated bubble (B_2) grows, it is elongated by the contraction of the first bubble (B_1) (see Figure 2b). The final moments of B_1 coincide with the start of collapse of B_2 which is accelerated by the second emitted pressure wave of B_1 causing the elongated cone to invert and form a focused jet [24,25] (refer to Figure 2c). B_1 completes its collapse and rebounds in the opposite direction. The direction of the narrow jet of B_2 can be predetermined from the axis of the two bubbles, whereas the speed can be modified by the relative bubble sizes, initiation times, and spatial separations. The target distance can also be varied to achieve different impinging areas and penetration lengths.

To efficiently compare the micro-targeting effectiveness of a double-bubble arrangement to that of a single-bubble, the effects of spatial and temporal parameters on double-bubble jetting speeds were explored. The relative bubble sizes could be expressed as the ratio $\rho = R_{max,2}/R_{max,1}$, where $R_{max,2}$ and $R_{max,1}$ represent the maximum radii that each bubble would reach in an isolated state. For simplicity, this study was conducted with same sized ~1 mm diameter bubbles ($\rho = 1$). First, the relative bubble-bubble (BB) initiation phase (τ) was fixed to analyze the effects of BB spatial separation on jet speeds. The BB initiation phase is defined by Equation 1,

$$\tau = \frac{\Delta t}{T_{exp,1}}, \tag{1}$$

where Δt is the temporal delay between the generation of each bubble and $T_{exp,1}$ is the

expansion time of B_1. Considering $\rho = 1$, T_{exp} is the same for B_1 and B_2 and equal to half of the bubble lifetime which can be measured from optical breakdown (i.e. plasma emission) to the end of bubble collapse [43]. The average bubble expansion time was $T_{exp} = 55 \pm 1.3$ µs. B. Han *et al.* numerically investigated jets produced by pairs of micro bubbles and described two distinct processes: in-phase ($\tau = 0$) and antiphase bubbles ($\tau = 1$). Using computational methods, they reported that for same sized micron-scaled bubbles ($\rho = 1$) a single optimal phase exists ($\tau = 1$) for producing fast jets regardless of BB spatial separation [24]. A change in the optimum BB phase is not expected for millimeter sized bubbles when compared to micron sized bubbles because the decrease in surface tension for larger cavities will affect the magnitude of the induced pressures not the time of pressure formation relative to the bubble collapse [44]. Thus, this study began with determining the optimum BB spatial separation for antiphase ($\tau = 1$) millimeter sized bubbles. The dimensionless spatial bubble-bubble separation (γ_{BB}) can be expressed as

$$\gamma_{BB} = \frac{D_{BB}}{R_{max,1} + R_{max,2}}, \tag{2}$$

where D_{BB}, is the spatial separation between the bubble initiation centers (see Figure 2a). The BB dimensionless separation is varied from $\gamma_{BB} = 0.55$ to 1.0 by translating one aspheric lens with respect to the other (f_1 and f_2, refer to Figure 1). After determining the optimum BB spatial separation, the effect of BB phase generation on the jet speed was confirmed by carrying out ten temporal delays in 5 µs increments. The phase experiments were conducted using the optimal BB spatial separation and a second arbitrary separation to experimentally test the dependency of the optimum BB phase on BB spatial separations.

Upon determining the optimum temporal and spatial conditions, the effects of the stand-off distance to a specified target on the damages produced were explored. The dimensionless bubble-target distance (γ_{BT}) is defined by

$$\gamma_{BT} = \frac{D_{BT}}{R_{max,2}}, \tag{3}$$

where the bubble-target (D_{BT}) spatial distance is normalized by the maximum radius of the closest generated bubble (see Figure 2c).

The resulting leading edge of the jets was tracked to estimate average speeds from the first sight of jet formation. Speed measurements via leading edge tracking provided low-end estimates because, there is a loss of liquid momentum as the gas drives the jet motion [12]. Upon finding the optimal BB parameters, the jets were directed towards soft paraffin and agar. Due to experimental limitations, the double-bubble arrangements for material targeting were reoriented on the Y-axis as seen in Figure 2. The soft paraffin and agar targets (i.e. samples) were immersed in the DI water on the top and floor of the cuvette respectively. The malleable soft paraffin was placed on the top edge to avoid smearing on the cuvette and preserve the sample's flat profile. The agar was placed on the floor of the cuvette as this position allowed for the highest stability of the sample. The target-cuvette assembly was translated by an XYZ stage to vary the position of the bubbles relative to the edge of the target. Cavities formed in soft paraffin were approximated as circular and characterized by the radii and penetration lengths using ImageJ to analyze images obtained using an optical microscope (20x magnification, Meiji Techno, Japan). The penetration lengths in agar phantoms were measured using ImageJ and high-speed image sequences.

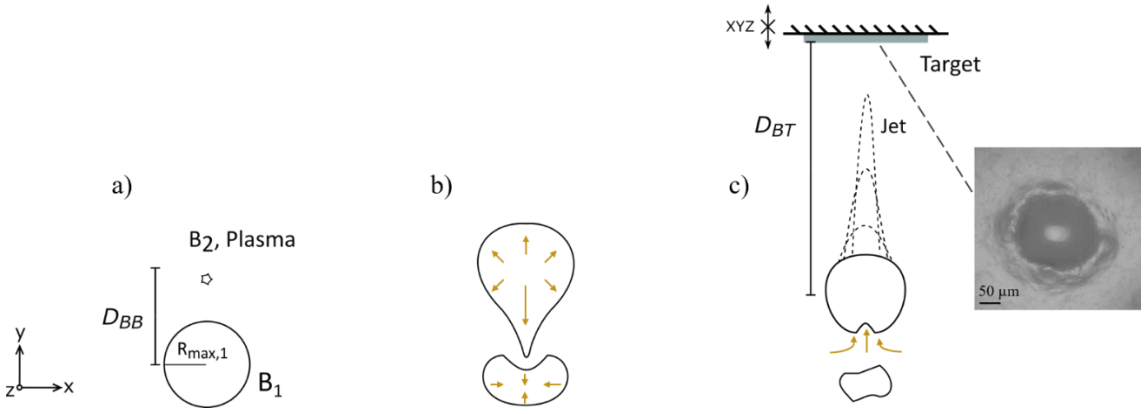

Figure 2-2: Camera point of view of target setup and depiction of DBJ process. a) Formation of B2 at maximum size of B1 with spatial separation DBB b) elongation of B2 formed by contribution of B1 collapse. c) Reversal of conical edge and propagation of jet. Inset shows damage on soft paraffin.

2.4. Results and Discussion

2.4.1. Effects of Bubble-Bubble Separation and Phase Initiation on Jet Velocity

The jet speeds are first studied at varying relative distances while maintaining the BB temporal delay constant at $\tau = 1$. The bubbles are isolated from boundaries at approximately $5R_{max}$ from the closest cuvette wall and oriented in the X-axis as seen in Figure 1. Figure 3 shows four sequences of antiphase bubbles interacting at BB separations of $\gamma_{BB} =$ 0.63, 0.74, 0.85, and 1.07. The captured images of bubbles and jets appear as black shadows due to the refraction of incoming light in the water-gas interface. To understand the formation of jets in antiphase bubbles, attention is first placed on the most defined case of $\gamma_{BB} = 0.74$ (see Figure 3b). In the case of antiphase bubbles, B_2 is initiated at B_1's maximum size and the overlap between B_1's collapse stage and B_2's growth stage forms an elongation in B_2 representing a conical shape towards B_1 (most

noted in Figure 3b at 15.5 μs). The inflow of liquid between the bubbles forms a high-pressure region as reported in the simulations of B. Han [24]. As B_2 begins to collapse, B_1 has completed its collapse stage and due to its rapid decrease in volume a high-pressure compressive wave is emitted [16,45] surrounding the tip of B_2 and further driving its collapse. The sharp coned-wall of B_2 inverts and collapses at a faster acceleration than the opposing bubble wall [44] causing a net radial inflow in which a jet forms and travels through the bubble in a toroidal shape piercing the opposite bubble wall. Simultaneously, an opposing unfocused bulk flow emerges from B_1.

When the bubbles are too close (Figure 3a) B_2 elongates asymmetrically during its growth, but its proximity causes it to penetrate through the walls of B_1 interfering with the jetting process due to the fractional coalescing of the two bubbles. Upon the start of collapse of B_2, however, the elongated curved edge still reverses and forms an outward unfocused flow as seen in Figure 3a, 46.4 μs onward. When the bubbles are more distant, as in Figure 3c, the stretching of B_2 occurs without physical contact with B_1, but the elongation is not maximized (see Figure 3c, 31 μs) and the interaction is weakened. As the bubbles are distanced further, as in Figure 3d, their behavior begins to resemble isolated cavitation events with minor opposing flows. The effect of the separation is easier realized by plotting the speed over time as seen in Figure 4.

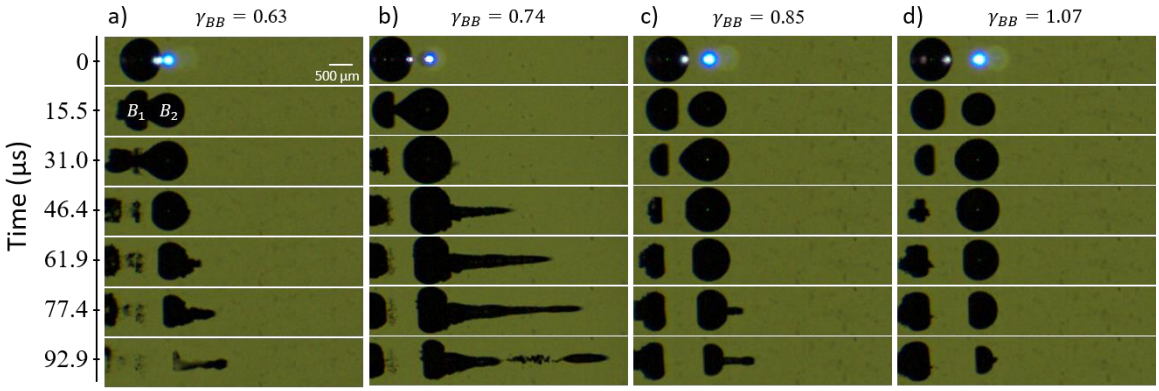

Figure 2-3: Image sequence of four bubble-bubble spatial separations: γ_{BB} = a) 0.63, b) 0.74, c) 0.85, and d) 1.07 (each at τ = 1). The first image (time 0) shows the moment that Laser 2 is fired.

Figure 4 plots the speeds of the emerging jets of Figure 2-3 starting from the first sight of bubble protrusion. At the furthest conducted separation of $\gamma_{BB} = 1.07$, no concentrated fluid motion is seen until after 90 µs of bubble initiation and thus, is not plotted. Figure 4a shows the jet evolution for the optimal BB spatial separation (refer to Figure 3b) and equal displacement of bubbles closer to and further from each other by a change of $\Delta\gamma_{BB}$ = 0.11. The overlapping profile speeds of 0.63 and 0.85 in Figure 4a suggest that the jet is diminished similarly for displacement above and below the optimum BB separation of $\gamma_{BB} = 0.74$. However, the jets do not emerge at the same time; smaller bubble separations produce jets at an earlier time due to the shorter distance the jet must travel to reach the opposite bubble interface. Figure 4b shows the maximum jet speed for different γ_{BB}. An optimal γ_{BB} occurs at 0.74, and the effect on BB separation appears symmetric for the range of this study. In this case, the maximum averaged measured velocity of U_{max}= 87.6 ± 9.9 m/s is achieved within 5 µs of jet formation and converges to U_{conv} ~25 m/s within

80 µs. We experimentally verified the assertions in Ref. [24] that antiphase bubbles (τ = 1) produce the fastest jets regardless of a different bubble scale and independent of BB separation. These experiments are included in Appendix A. The BB separation and phase are kept constant at $\gamma_{BB} = 0.74$ and $\tau = 1$ for the remainder of the experiments.

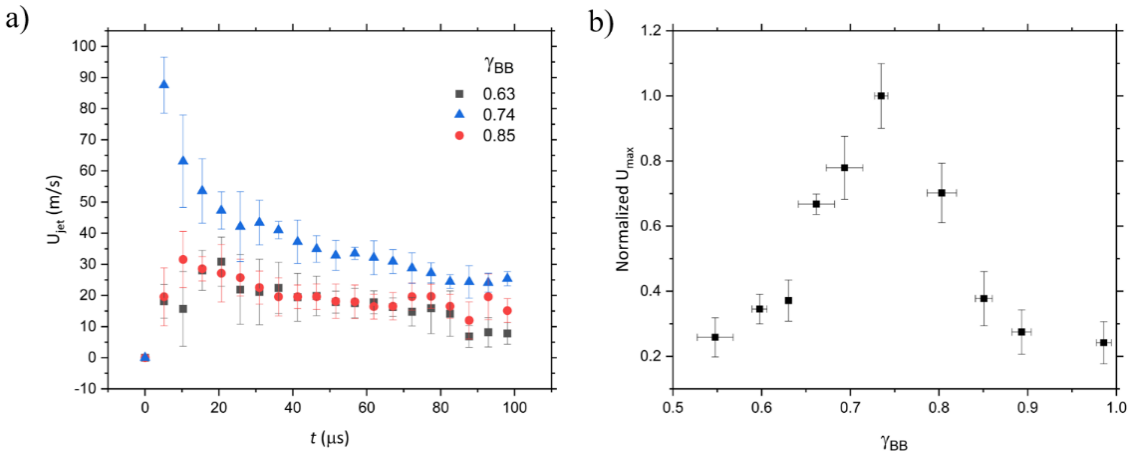

Figure 2-4: a) Jet speed with respect to time of jet formation for three different BB separations (γ_{BB}) at τ = 1, ρ = 1. b) Normalized maximum jet speed for various BB separations.

2.5. Penetration Length and Damage Radius vs Bubble-Target Stand-off in Soft Paraffin

To demonstrate the extent that DBJ can outperform SBJ in existing applications such as surface cleaning or cell targeting, sites generated by each configuration's jets impinging onto a soft paraffin were compared. As mentioned in section 2, the bubbles were reoriented onto the Y-axis. The effect of gravity is negligible as shown by the Froude number (ratio of inertial and gravitational forces), U_{jet}^2/gL, where U_{jet} is the jet velocity, g is the acceleration due to gravity and L is the characteristic length. Taking the jet velocity as the optimum converged speed (U_{conv} ~25 m/s) and characteristic length as the length of the jet

at the furthest measured point (L = 1.75 mm), the Froude number is on the order of 35 x 10^3 which confirms that the jet's inertial forces are dominant for the specified scales. Additionally, experimental tests of Y and X-axis BB orientations produced comparable average jet speeds within uncertainties of the measurements (Y jet speeds are not shown).

Figure 5a and 5b show dynamics and damages of SBJ and DBJ impingement onto soft paraffin, each reaching comparable penetration lengths of roughly 110 μm. The sequences show three moments: 1) the maximum bubble growth (B_2 in DBJ arrangement), 2) the time of impact onto the soft paraffin, and 3) the maximum size of the rebound bubble. The resulting damages are fitted to a circle and characterized by the radius as seen in Figure 5a. In each arrangement, the jet removes clusters of material upon impact, but due to the properties of the soft paraffin and the radial shear outflows at the material surface, the jet primarily pushes the material outward creating a raised ring-like shape. By comparing the point-of-impact images (Figures 5a, @ 61.2 μs and 5b, @ 32 μs), the difference in jet widths upon impingement is noted; DBJ results in a finer jet. The difference in the jet dimensions can be attributed to the curvature of the bubble before the jet is formed (may also be affected by distance to target). The dashed lines in Figures 5a and 5b at 0 μs outline the curvature of the opposite bubble wall which inverts in a toroidal shape and becomes the leading edge of the jet. The asymmetrical geometry of each case (boundary on one side for SBJ and bubble on the opposite side for DBJ) cause an elongated growth and due to surface tension, the bubble walls with the highest curvature implode faster[17]. The feature of higher curvature in DBJ seems to lead to a finer jet capable of larger penetration lengths than SBJ as seen in Figure 6. The rebound bubbles also play a role in the formation of the

damage. Particularly in SBJ cases near $\gamma = 1$, following the first collapse of the cavitation bubble, the rebound is attached to the target and the bubble regrows highly asymmetrically along the wall (see Figure 5a, 79.2 µs), further enlarging the damage radius. This rebound damage contribution is not present in the case of DBJ because the successive regrowth and collapse occur off-site away from the surface (noted in Figure 5b @ 80 µs).

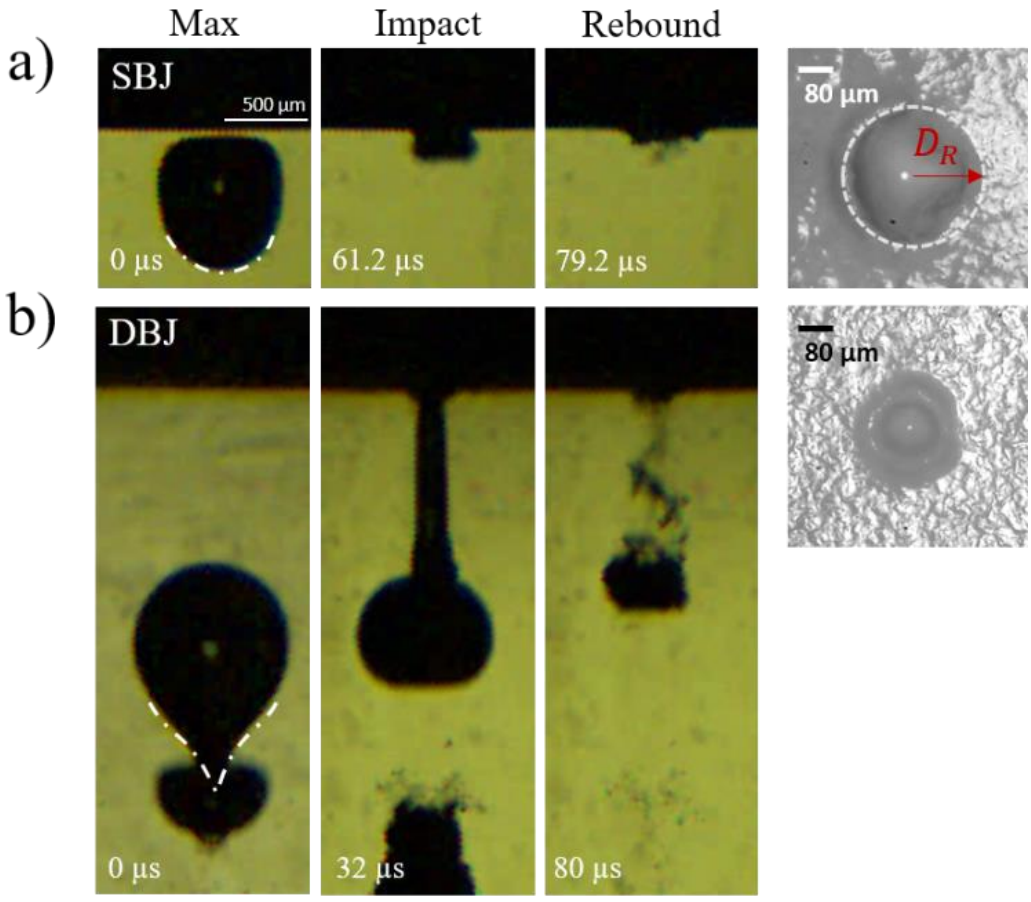

Figure 2-5: Jetting dynamics and soft paraffin damage radius for a) single ($\gamma = 0.96$) and b) double-bubble jetting ($\tau = 1$, $\rho = 1$, $\gamma_{BB} = 0.75$).

Figure 6 shows the penetration length (L_P) and damage radius (D_R) for both SBJ and DBJ at various bubble-target stand-off distances. Damage sites resulting from single

bubbles can be observed up to approximately $\gamma_{BT} = 1.4$, in which both the damage lengths and radius from single bubbles follow a similar trend: the values increase parabolically as the stand-off distance approaches a value of $\gamma_{BT} \approx 1.1$. After $\gamma_{BT} \approx 1.1$, the lengths and radii begin to decrease. In the range of SBJ experiments, the damage radius is consistently larger than the penetration lengths achieved which may be unfavorable for various applications such as needle-free injections. The effect of using DBJ for inducing damage sites shows two notable differences when compared to SBJ damage sites. First, DBJ can produce damages at larger stand-off distances up to $\gamma_{BT} = 4.2$. Additionally, in the range of ($1.75 < \gamma_{BT} < 3.8$), the damage radii are smaller than the penetration lengths thus generally making DBJ a more suitable technique for localized targeting in scenarios that require smaller impact radius-to-length ratios. Stand-offs outside this range generate similar damage sites as those seen SBJ, that is, the damage radii surpass the penetration lengths. As the stand-off is decreased from $\gamma_{BT} = 1.4$, both the damage radii and penetration lengths begin to decrease following a similar trend as $\gamma_{BT} < 1.1$ for SBJ. As the DBJ arrangement is moved closer to the soft paraffin target, a larger portion of the jet (radially out from the central axis) has sufficiently high velocity to deform the target in a larger region. Additionally, a vortex flow occurs when the jet impinges on the target which provides a shear stress that further enlarges the damage radius. In the largest observed stand-offs, the average damage radius and penetration lengths are within uncertainty. In the specific case of Figure 5a and 5b, the damages of each configuration are compared. To achieve the same average penetration length of approximately 110 μm, γ_{BT} of double-

bubble jetting can be on average 3 times larger than that of single bubble jetting. Additionally, the damage surface profile is about 45% smaller for the DBJ configuration.

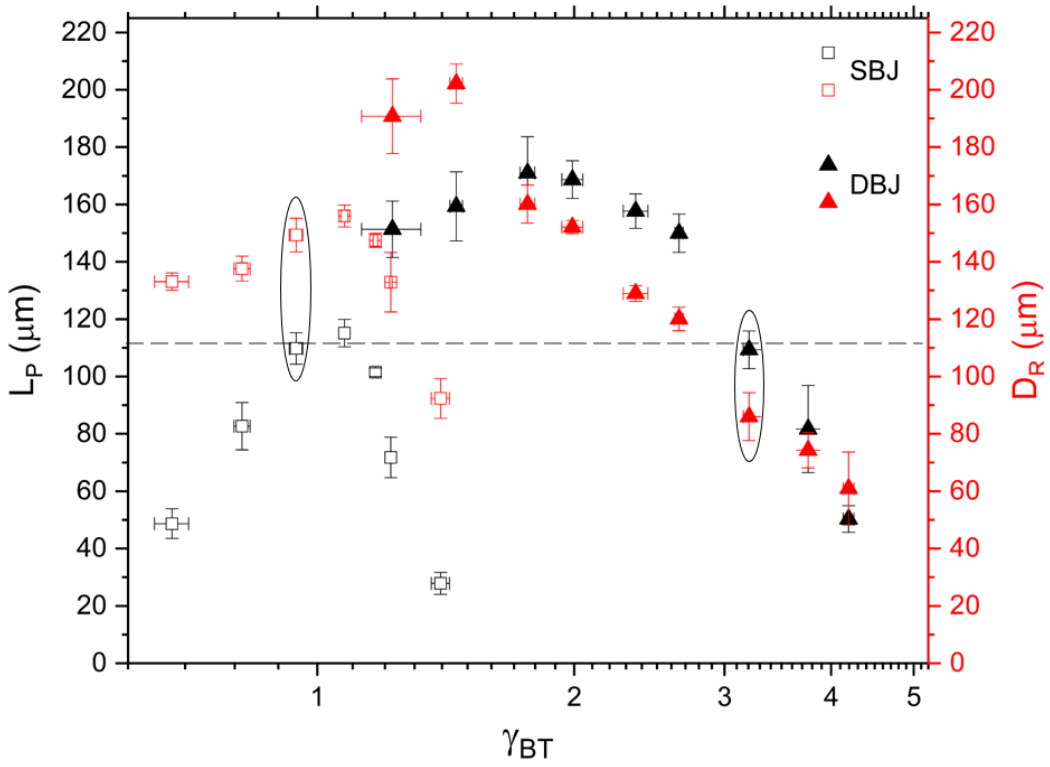

Figure 2-6: Penetration length and damage radius for single- and double-bubble jetting at varying bubble-target distances. Dotted line runs across similar-sized penetration lengths for cases in Figures 5a 5b. Measurement of penetration length starts from initial surface base.

2.6. Penetration Length vs Number of Jet Impingements in Agar-gel Phantom

To observe the effect of multiple successive jets from a double-bubble jetting arrangement, emerging jets were directed towards soft paraffin and an agar-gel phantom. Figure 7a shows lateral sequences of jet propagation into agar for different number of jets (J_i, where i = 1, 3 and 5 jets) on the same spot. The jet is first seen to penetrate the agar in J_1, at 10.4 µs and propagates through 41.6 µs. Upon penetrating the agar interface, the jet's

shadow appears thinner as only the core of the jet provides enough pressure to cause failure in the agar. However, in subsequent jets J_3 and J_5, the propagating jet inside the agar is notably wider due to the preexisting guide of cavities formed from previous jets. Additionally, the jet penetrates further after each successive jet. In all cases, upon the collapse of B_2 (Figure 7a, row 41.6 μs), the jet inside the agar seems to vanish. The gaseous blanket surrounding the jet has condensed and recombined with the liquid whose refractive index closely matches that of the agar target.

Figure 7b shows the penetration lengths achieved with various successive number of jets for double-bubble jetting onto agar and soft paraffin. The experiments are conducted in the soft paraffin with the purpose of showing the trend in a different material. Each point in the plot corresponds to the average penetration length achieved by three repetitions of different number of jets varying between 1 jet to 8 jets. The temporal separation of subsequent jets is on the order of about 10 seconds, large enough for initial conditions to restore after each jet. A stand-off of $\gamma_{BT} = 3.5$ was chosen for both materials as it is sufficiently distanced enough to allow for estimating the impact jet velocity, but not large enough for the penetration area to have a large aspect ratio (radius/penetration length) as seen in Figure 6. A linear relation can be fitted onto both materials up to the first 5 jets, with a slope of 250 μm/jet and 40 μm/jet for agar and soft paraffin respectively. The first jet punctures the agar with a pilot cavity which then serves as a guiding channel for successive jets. The penetration length is approximately linear during the first 5 jets and begins to plateau with additional jets generating smaller growths. The plateau can be attributed to keeping the base plane constant, regardless of the local γ_{BT} stand-off distance

increasing in the impact region after each jet. After 5 jets, the flow's momentum is decelerated resulting in smaller and more variable impact pressures as seen in the corresponding growth of the standard deviations in Figure 7b. At larger number of jets, the length will remain constant unless the bubble-target distance is readjusted after each jet. The plot for soft paraffin, although not achieving the same lengths, provides a similar linear trend for approximately the first 5 jets.

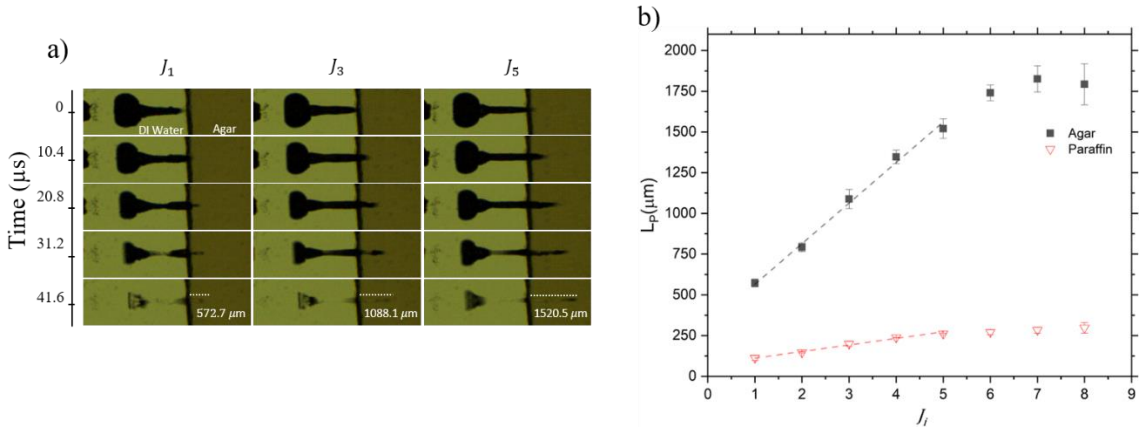

Figure 2-7: a) Lateral view of jet propagation in 1% agar using J_i = 1, 3 and 5 DBJ jets in the same region. b) Penetration length on agar and soft paraffin as a function of number of impacting jets (J_i) (τ = 1, ρ = 1, γ_{BB} = 0.75, γ_{BT}= 3.5). Each point in the plots represent the average of 3 experiments.

Although the effect of the jet can be quantified by the resulting penetration lengths and damage radius, the principal contributors to the effects achieved are the jet velocity, and elastic modulus of the target. The impact pressure P_{jet} of the jet that causes the failure in the sample is calculated by

$$P_{jet} = \frac{1}{2}\delta U_{jet}^2, \tag{4}$$

where δ is the water density, and U_{jet} is the jet velocity [46]. The mechanical stress applied by the jet pressure must exceed the elastic modulus (E) of the target of interest for failure to occur. K. Cu *et al.* defined the penetration strength ratio $S = P_{jet}/E$ to indicate the potential of target rupture (if S > 1) [47]. At a stand-off of γ_{BT}= 3.5, the DBJ average impact velocity is U_{jet} = 32 m/s and provides an impact pressure of 512 kPa, and an approximately penetration strength ratio of 25 for a sample of 1% agar. Such penetration strength signifies that the discussed setup can afford to penetrate a stiffer material, or the stand-off distance may be further increased.

The cavities formed in the agar phantoms can be approximated as conical shapes to estimate the injection volumes achieved. For J_5, the radius of the cavity D_r (measured from the images in Figure 7), is approximately 125 μm at the entrance (measured at 20.8 μs because of higher contrast) and the penetration length is about 1.52 mm. Using the volume of a cone, $V = L\pi {D_r}^2/3$, where L is the penetration length, and D_r is damage radius of the cavity, the approximate injected liquid amounts to 25 nL (or 5 nL per jet until 5 jets) which is on the lower-end for required dosages of typical applications (vaccines, antibiotics [48]). To compare the effectiveness of this technique with other needle-free methods, the injection efficiency, defined by the ratio of jet kinetic energy to the input energy required to generate the jet, is found. Table 1 compares the performance of DBJ to other laser-based injection methods.

Table 1: Comparison between laser-based injection systems.

Method	Apparatus	U_{max} (m/s)	Volume/Penetration per Injection	ϵ_{energy} % [a]	Energy (mJ)	Ref.
Thermocavitation (450 nm, 0.5 W, 1 ms)	Chamber: D 120 µm, L 700 µm Nozzle: D 120 µm	-	20.2 nL/ 1.2 mm	0.32	5	[35]
Pulsed cavitation and ablation (2940 nm, 1085 mJ, 150 µs)	Chamber: H 11 mm Nozzle: D 150 µm	120	350 nL, 3.5 mm (10 % polyacrylamide gel, ~60 kPa)	0.21	1085	[49]
Thermocavitation (790 nm, 116 mW, 500 ms)	Chamber: D 120 µm, L 200 µm Nozzle: D 50 µm	94	~40 nL/ 675 µm (1% agarose, ~15 kPa [50])	0.07-0.14	58	[30]
Pulsed cavitation (1064 nm, 1 mJ each, 6 ns)	None	87	~5 nL/ 570 µm (1% agar, ~20 kPa [41])	0.13	2	This work

[a] Injection efficiency: jet kinetic energy transferred to the material per energy supplied to injectors [35]. $\epsilon_{energy} = {KE}/{E_{laser}}$.

As seen in table 1, the injection efficiency by energy is on the lower limit of other laser-based injection systems. However, this efficiency depends on the modulus of the sample, which is lower than those in references [35,49] but higher than reference [30]. One advantage of DBJ over previous laser-based jetting systems is the absence of required microfabricated devices. Such complex microchannels and nozzles are prone to clogging which can

decrease jet controllability overtime. Moreover, existing continuous wave systems superheat the jetting fluid for several microseconds before cavitation is initiated[9,37], possibly changing the molecular structure of medication. Such issue is limited to short lived and localized heating[40], but can be further avoided by generating the double-bubble jets in a separate medium and transferring the momentum to the medicine. Additionally, to further enhance the injection efficiency of DBJ to be useful for needle-free injection purposes, the addition of tapered nozzles could be explored. However, due to the fast jets without additional apparatus, such added nozzle would not be required to be micron-scaled as those in table 1 and thus less prone to damage.

2.7. Conclusion

We analyzed the microjet effect on soft materials due to spatial and temporal separation between a double-bubble arrangement. The dynamics of two neighboring bubbles are explored to compare the effectiveness in which double-bubble jetting (DBJ) may be more beneficial in applications of localized targeting that currently use a single-bubble jetting (SBJ). A double-bubble arrangement allows for higher degrees of freedom for controlling jet dynamics when compared to only one parameter with single-bubbles. The critical parameters of bubble-bubble temporal and bubble-bubble spatial initialization were found to be $\tau = 1$ and $\gamma_{BB} = 0.74$, respectively. The phase of $\tau = 1$ allowed for the same sized bubbles to align B_1's pressure emission upon collapse with the beginning of B_2's collapse which formed a constructive interaction leading to an average maximum jet velocity of $U_{jet} = 87.6\ m/s \pm 9.9\ m/s$ At the critical BB separation, the bubbles were close enough

to have a strong, constructive interaction with the present pressure fields, but far enough to not interfere with the other bubble's dynamics. With these critical conditions, DBJ proves to be superior to SBJ when considering penetration lengths versus impact region. The same penetration length in soft paraffin can be achieved using single and double-bubble jetting, but at safer (~3x larger) stand-off distances and minimized surface damages (by about 45%) for double-bubble configurations. Particularly, the advantages of DBJ over SBJ can be attributed to two contributing features. First, the DBJ arrangement seems to lead to a sharper elongation translating to a finer jet upon impingement. Additionally, due to larger initial target separations in DBJ, the rebound bubble does not reach nor contribute to the damage site. Further, the DBJ configuration was directed onto a 1% agar-gel phantom as a proof of concept for needle-free applications. Successive jets into the gel led to a linear increase in the penetration length up to 1.5 mm after 5 jets with a volume of 25 nL. Double bubble arrangements may be compact, device-free alternatives for needle-free applications, but further studies are required to fully understand the resulting process. Particularly, the degree and effect of possible vapor entrainment into the formed cavity is not understood. Furthermore, factors governing jet formation namely, relative bubble ratios, solution surface tension and viscosity remain to be studied to determine their effects on achieved penetration lengths.

2.8. Additional Information

Acknowledgements

The authors would like to thank Juan Carlos Gonzalez Parra for laboratory assistance and fruitful discussions. V. Robles was funded by the Ford Foundation Predoctoral Fellowship.

Data

The data that supports the findings of this study are available within the article.

Appendix A

Figure 8 shows typical jet evolutions of four phase separations (τ = 0, 0.54, 1, and 1.44) at a BB spatial separation of γ_{BB} = 0.74. For simultaneous generations, as seen in Figure 8a, each bubble behaves like a single bubble acting on a nearby solid boundary. That is, the bubbles are attracted to each other, but in distinction, a thin liquid layer is formed between the gaseous cavities until coalescing occurs at the beginning of the rebound bubbles (Figure 8a @ 154.8 μs). No outward focused jet formation is observed due to the destructive interference of the equal and synchronized opposing pressure waves.

As the phase difference increases from τ = 0, as seen in Figure 8b, the flow changes from two inward bulk motions to two repelling flows. The temporal gap allows for the partial overlap of B_1's growth and B_2's collapse leading to the formation of the conical shape in B_2 that reverses into its own walls and generates a sharp outward flow. Further

increase in the phase until τ = 1, (Figure 8c), concentrates more mass flow in one direction, and B_1's flow becomes more defined while the opposing side remains a slower bulk flow. When B_2 is initiated at B_1's maximum size (Figure 8c @ 56.8 µs), the bubble becomes elongated as with a smaller phase difference (Figure 8b), but the arrangement allows for a stronger effect. Further increasing the BB phase past τ = 1 (Figure 8d) decreases the strength of the formed jet due to a shorter exposure to the high pressures generated during the alignment of B_1's collapse and B_2's maximum size. A notable difference between an approximately equal positive and negative phase shift from the optimum antiphase arrangement, is on the shape of the jet. For jet-forming phases smaller than τ = 1, the jet has a focused, pointed shape which can propagate at faster speeds most notable in Figure 9 which shows the jet evolution over time and maximum speeds achieved at variable BB phases.

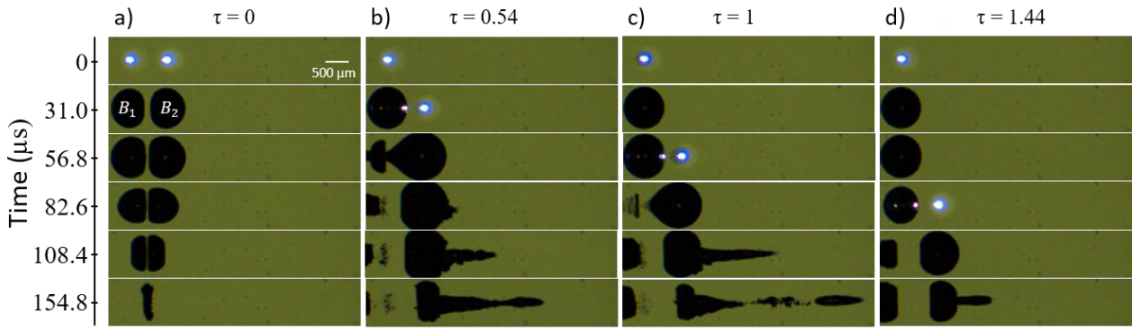

Figure 2-8: Image sequence of four different phase separations: τ = a) 0, b) 0.54, c) 1, and d) 1.44 (each at $\gamma_{BB} = 0.74, \rho$ = 1). Time 0 shows the moment that Laser 1 is fired.

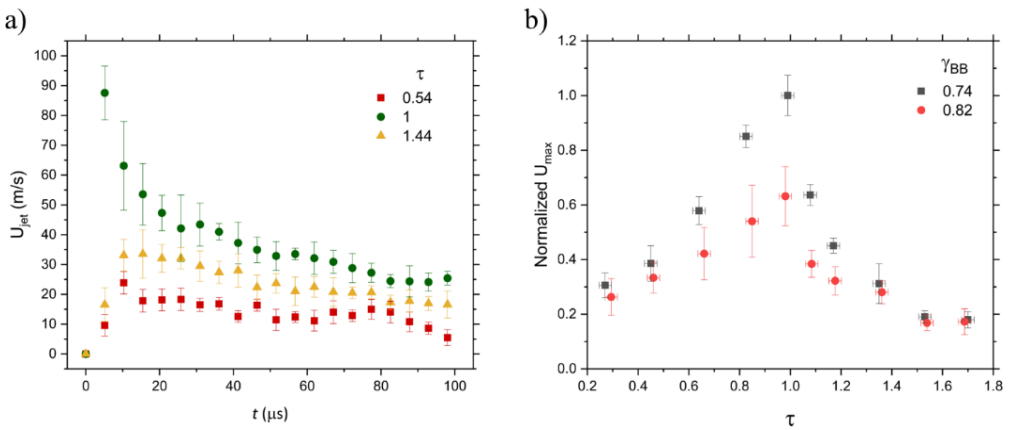

Figure 2-9: a) Jet speed with respect to time of jet formation for three different BB initiation phases (at $\gamma_{BB} = 0.74, \rho = 1$). b) normalized maximum jet speed for various bubble-bubble phase separations.

The three phases shown in Figure 9 are chosen for representing the peak jet speed reached at $\tau = 1$, and comparable delays of $\Delta\tau \approx \pm 0.45$. As observed in Figure 9 a, a delay before and after the optimal phase do not lead to the same diminishing effects. A shorter delay leads to a higher converged velocity (U_{conv}~18 m/s) than the same displaced delay above the optimal phase (U_{conv} ~11 m/s). This may be explained by the different pressure conditions during the formation and propagation of the jet. For jets formed at phases smaller than $\tau = 1$, the growth of B_2 coincides with the full collapse of B_1 and is thus pulled and elongated. For jets $\tau \geq 1$, the growth of B_2 partially overlaps with both the collapse and regrowth of B_1. Thus, B_2 is not maximally elongated, and the emerging jet is not accelerated at the same rate. This suggests that to minimize change of speed from errors, it is best to underestimate the expansion time and be to the left of the optimal point. Differences can be further noted by comparing the time constants of the exponential growth, $C_{growth} =$

0.53, and exponential decay, $C_{growth} = 0.26$. The phase of τ = 1 has the largest velocity error bar because the jet tip of the highest speeds can be within the bubble shadow and emerge at variable times for each experiment.

Chapter 3. The Effect of Scalable PDMS Gas-Entrapping Microstructures on the Dynamics of a Single Cavitation Bubble

Vicente Robles[a], Juan Carlos Gonzalez-Parra[a], Natanael Cuando-Espitia[b], and Guillermo Aguilar[a,c]

[a]*Department of Mechanical Engineering, University of California Riverside, CA 92521, USA.*
[b]*CONACyT, Applied Physics Group, DICIS, University of Guanajuato, Salamanca, Guanajuato 368850, México.*
[c]*J. Mike Walker '66 Department of Mechanical Engineering, Texas A&M University, College Station, Texas 77843, USA.*
**Corresponding author: aguilar@tamu.edu*

Abstract

The effect of gas-entrapping polydimethylsiloxane (PDMS) microstructures on the dynamics of cavitation bubbles laser-induced next to the PDMS surface is investigated and compared against the cavitation dynamics next to a flat smooth boundary. Local pressure gradients produced by a cavitation bubble cause the air pockets entrapped in the PDMS microstructures to expand and oscillate, leading to a repulsion of the cavitation bubble. The microstructures were fabricated as boxed crevices via a simple and scalable laser ablation technique on cast acrylic, allowing for testing of variable structure sizes and reusable molds. The bubble dynamics were observed using high speed photography and the surrounding flows were visualized and quantified using particle tracking velocimetry. Smaller entrapped air pockets showed an enhanced ability to withstand deactivation at three stand-off distances and over 50 subsequent cavitation events. This investigation provides insight into the potential to direct the collapse of a cavitation bubble away from

a surface to mitigate erosion or to enhance microfluidic mixing in low Reynolds number flows.

Keywords: laser-induced cavitation, gas-entrapping microstructures, hydrophobic surface deactivation

3.1. Introduction

Cavitation bubbles, particularly induced via lasers, have recently become the focus of numerous studies for their precise control in the micro spatial and temporal scales making them favorable in microfluidic applications. The influence of nearby rigid boundaries (i.e. solid walls) on cavitation dynamics has been comprehensively explored and can be generally understood as attracting a cavitation bubble and forming a microjet centered in a toroidal-shaped collapse [44]. The interaction studies of cavitation near solid walls have expanded to studies with other boundaries including rigid corners, edges, parallel walls, crevices, and enclosed microfluidics [31,51–54]. Even more, as the interactions of cavitation bubbles with stationary boundaries become better understood, transient interactions are being explored. For instance, Brujan et al. found that depending on the stand-off distance (γ, distance of bubble center to a surface normalized by the bubble's maximum radius) a cavitation bubble collapsing near an elastic boundary can experience a repulsion, attraction, or reversal of direction depending on the material's elasticity [20]. Additionally, the interaction of cavitation bubbles near a free surface and inside a droplet has also been reported for an additional directional control of the jet formed during collapse [55,56]. In our previous investigation of employing neighboring cavitation bubbles, we showed the

potential for needle-free injections by further controlling of the microjet velocity depending on the bubbles' temporal and physical separations [57]. In each of the studies, the cavitation process has been limited to a single bubble interacting with either static boundaries, or with a single dynamic interface. Additional nearby interfaces will complicate the cavitation dynamics but may enhance the efficiency for which cavitation has found applications in such as for microfluidics [58–60], or potentially surface cooling [61].

Recently, S. R. Gonzalez Avila et al. proposed the use of gas-entrapping microtextured surfaces for mitigation of cavitation erosion. In this study, they showed that in a hydrophobic surface with an array of gas-entrapping microstructures, a collapsing cavitation bubble can migrate away from the surface due to the protrusion of the surface-entrapped air pockets that expand during the tensile pressure caused by the cavitation collapse [62]. Moreover, the authors explain that such dynamics of entrapped gasses can help mitigate cavitation damage on a surface by directing the bubble away and eliminating the jet impact and rebound collapses that have been shown to contribute to surface erosion [63–66]. One of the challenges highlighted in their work was the relatively rapid wetting transition from a dry Cassie-Baxter state to a Wenzel state where the surface becomes "deactivated" and the previously air-filled microstructures become filled with water. Upon detachment of the air pockets, the effective hydrophobicity is reduced, and the crevices fill with water leading to a smooth-like surface and diminishing the repulsion properties on subsequent cavitation bubbles. In an earlier study, Borkent et al. found that nucleation of a superhydrophobic crevices (hierarchal structures micron pits superimposed with nanopillars), could be activated over 200 times by incident pressure pulses [67]. That is, the

additional surface roughness of the crevices helped the air pockets remain intact without affecting the surface's wettability as drastically as observed in [62]. Additionally, another study also found that an increase in surface roughness and decrease in microstructure pitch (from 460 to 55 μm) can result in enhanced contact angles for different materials [68].

In this work, we investigate the degree to which variable sized gas-entrapping microstructures affect the dynamics of and resulting flow following a laser-induced cavitation event. Our surface structure arrays are formed in a relatively simple and scalable method of polydimethylsiloxane (PDMS) castings from laser-ablated cast acrylic. The laser scribing process naturally provides an extra peak feature and the hydrophobic properties of the PDMS enhance the entrapment of air pockets. With sufficient stabilization of the entrapped air pockets, heterogenous nucleation could be efficiently used for more than mitigation of erosion. For instance, the temporarily protruding gasses may actively agitate stagnant or laminar flow by amplifying the turbulent effects of a single cavitation bubble [69]. Further, this method could also allow superhydrophobic surfaces to utilize enhanced properties of drag reduction with low friction air-pockets, while allowing for on-demand localized mixing or other micro-manipulation operations such as rotation of cells and valveless pumping.

3.2. Materials and methods

3.2.1. Microstructure fabrication and wettability characterization

The gas-entrapping microstructures were casted onto polydimethylsiloxane (PDMS) using acrylic molds. PDMS castings were chosen as a cost-effective and simple alternative

in contrast to more complex techniques such as molecular vapor deposition and photolithography. The use of PDMS allowed for multiple sample preparations with a well-established material in the microfluidic fabrication field. Additionally, PMDS has natural hydrophobic properties, which assisted in further increasing the entrapment of air pockets and is widely used in biophotonic applications due to its transparency and biocompatibility properties [70]. The molds were processed on cast acrylic (McMaster-Car, 8560K171) sheets and scribed in 5 x 5 mm^2 areas via laser ablation using a 1030 nm Ti:Sapphire laser (Amplitude Systèmes, Satsuma HP3) delivering 350 fs pulses at a fixed rate of 1kHz. A 5x microscope objective was used to focus the laser pulses which averaged a power of 30 mW. The acrylic samples were placed normal to the incident beam and translated on a motorized stage at a constant velocity of 0.6 mm/s to ablate the negative pattern. As depicted in Figure 1a, the three acrylic samples were patterned as a grid of 20 μm wide channels (tapering to a point), separated by a pitch of 100, 150 and 200 μm (labeled β_{100}, β_{125}, and β_{150} respectively). These dimensions were selected to allow for multiple structures in the vicinity of the cavitation site and because previous works have shown gas-entrapment with similar micron-sized structures [62,71]. The scribed negative molds were then cleaned with isopropanol alcohol to remove residue, rinsed with deionized (DI) water, and dried prior to PDMS casting. Then, PDMS (Krayden, 184 Slygard) was prepared in a 10:1 ratio with curing agent, thoroughly mixed for 10 minutes and degassed in a vacuum chamber for 5 minutes to eliminate bubbles before pouring on the molds. The PDMS mixture was poured onto the acrylic molds with constraining walls to form the PDMS samples with a thickness of 3 mm. The uncured PDMS was then covered with a microscope slide and left to cure

overnight. To ensure that the PDMS was completely cured, it was further baked for 3 hours at 47 °C followed by careful removal from the mold. After curing and removal, the resulting PDMS structures were analyzed using SEM to verify proper casting. Figure 1b shows SEM images of each acrylic laser-scribed mold and their PDMS casted counterparts (below). The microstructure walls measure approximately 45 µm in height. As seen in the PDMS castings, small conical shaped peaks (~20 µm tall) are formed at the intersections due to the two-passes during laser ablation. A smooth PDMS sample (i.e. untreated) was fabricated using the same procedures, without a scribed pattern on the acrylic (not shown).

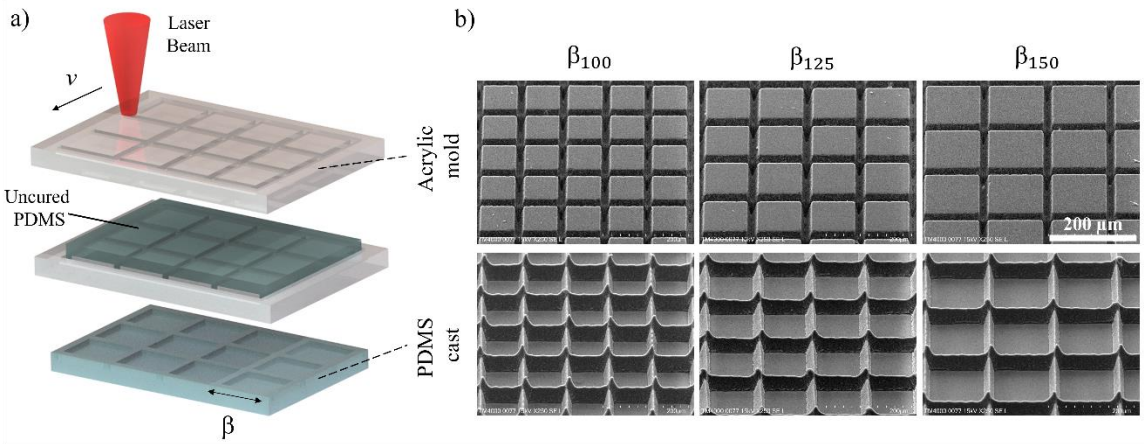

Figure 3-1: a) Schematic of microstructure fabrication process b) SEM images at 45° tilt of negative acrylic molds (top row) and cured PDMS casted microstructures (bottom row). Scale bar (200 µm) is uniform across images.

To characterize the ability of the PDMS microstructures to entrap air pockets upon water submersion, we analyzed the wettability properties for each grid size and compared them to the untreated PDMS surface. The sensile water droplet (SD) method was used to

measure the hydrophobicity relationship to grid size. Using a micropipette, a DI water droplet of 10 µL was carefully placed atop each sample until the droplet contacted the structured surface. The pipette was slowly removed such that the droplet remained on the sample without dropping. An image was taken immediately after, capturing the lateral view of the droplet on the surface as seen in Figure 2a. The sample was then dried with compressed air before repeating the experiment two more times for an average value of three contact angle measurements for each sample. The contact angle was measured using ImageJ and taken at the three-phase line interface (air-water-PDMS). As seen in Figure 2b, the untreated PDMS sample has the smallest water droplet contact angle of 108 ± 3° while decreasing the microstructure size, β, leads to an increase in contact angle. The smallest structure size of β_{100} has the largest contact angle of 161 ± 3°, suggesting it is the most hydrophobic sample of the tested surfaces.

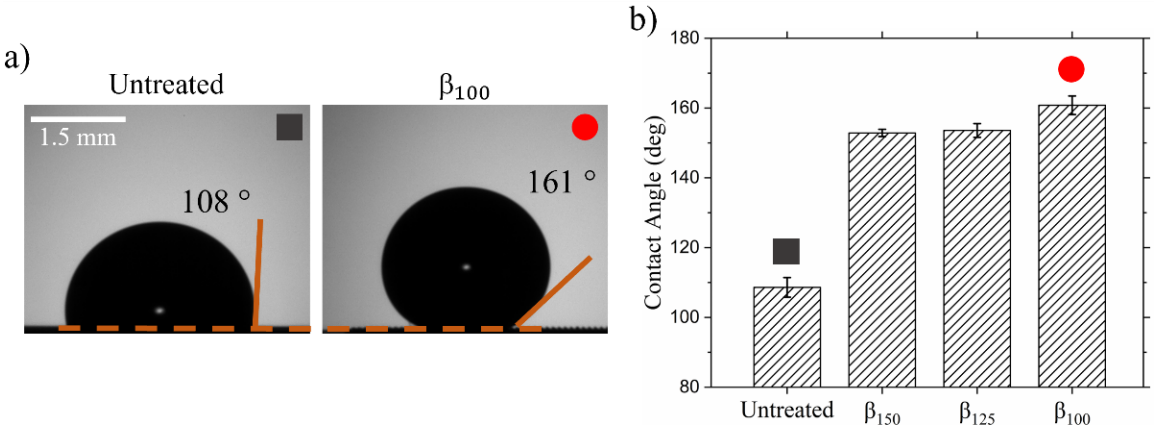

Figure 3-2: a) Visual comparison of sensile DI water droplet on a smooth, untreated PDMS and on the β_{100} microstructure sample. b) average of three contact angle measurements for each of the four samples studied.

3.2.2. Cavitation experimental setup and flow visualization

To observe the interaction between the entrapped air pockets (EAPs) in the PDMS microstructures and a cavitation event, we employed a Q-switched Nd: YAG laser emitting at 1064nm (Continuum, Surelite SLII-10) to generate cavitation in (DI) water. The cavitating laser was focused into a glass cuvette containing the DI water-immersed samples. The cuvette was placed on a 3-axis stage with a 10 μm resolution to allow for precisely varying the cavitation stand-off distance. Each experiment was conducted with energies of approximately 1 mJ which provided 100% bubble formation probability per pulse and formed an average maximum bubble radius, R_{max}, of 1.1 mm ± 9.8 μm (averaged over 5 events), lasting 100 μs ± 5 μs. The bubble interactions were captured using high speed (HS) shadowgraphy at 100,000 frames per second (fps) and 128 x 208-pixel resolution using a HS camera (Photron, Nova S6) coupled with a long-distance microscope (Infinity, KC VideoMax). As shown in Figure 3, an additional CCD camera was also mounted to provide a top view of the microstructures during experiments. A pulse delay generator (Berkeley Nucleonics, M-555) was used to externally synchronize and trigger the laser and HS camera up to a 1 ns resolution.

To visualize the flow fields following the interaction between the entrapped air pockets and a cavitation bubble, tracer particles were suspended in the DI water for particle tracing velocimetry (PTV) analysis. PTV was performed separately, independent from the primary experiments. The particles used for PTV were fluorescent green polyethylene microspheres (Cospheric, UVPMS-BG, ρ = 1.00 g/cc, 27-32 μm diameter) with peak excitation and emission at 414 nm and 515 nm respectively. The particles were excited by

a continuous wave (CW) 450 nm laser diode which was focused through a plano-concave cylindrical lens (f = -100 mm) to form a planar light sheet parallel to the HS camera sensor and centered at the plane of bubble formation. The HS camera captured the flow of the particles which was representative of the surrounding density-matched DI water. A long-pass filter (Thorlabs FEL0450) blocked the light from the CW diode such that the HS camera only captured the emission of the fluorescent particles and not reflection of the CW laser emission at 450 nm. Figure 3 shows a schematic of the main components in the experimental setup as described.

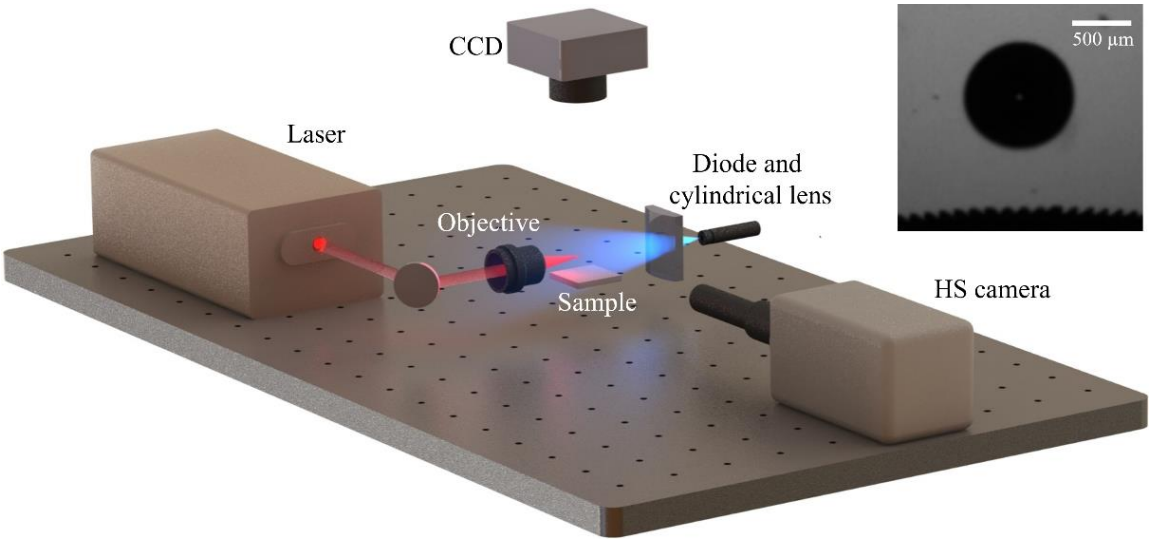

Figure 3-3: Schematic representation of the experimental setup to induce cavitation, record the bubble dynamics and perform PTV visualization. Inset shows representative HS image of a cavitation bubble above a microstructured surface.

3.3. Results and Discussion

3.3.1. Single cavitation bubble dynamics near microstructures

To observe the effect of the microstructures on the cavitation dynamics, experiments were conducted atop each pristine sample (i.e. freshly dried and submerged in DI water) including the untreated PDMS target as a control to compare against. Three stand-off distances (γ = 1, 2, 3) were used to determine the degree of bubble migration toward or away from the surfaces for "close", "mid" and "far" target distances. Three experiments were conducted at each stand-off distance for each sample and recorded for a duration of 2 ms at 100,000 fps with a 128 x 208-pixel resolution. During experiments, the cavitation bubble was centered on both the PDMS samples and within the cuvette to minimize asymmetrical conditions that may have influenced the bubble motion in the x-axis.

Figure 4 shows the representative bubble dynamics of a single cavitation event atop each structure at a stand-off distance of γ = 1. The first column of images ($t = 0\ \mu s$) represents the time of pulsed-laser irradiation as noted by the plasma flash. In Figure 4a, the case of a cavitation bubble collapsing near the untreated sample (Unt for short) behaves as expected with the bulk bubble volume being attracted towards the PDMS boundary during the collapsing stage. While the elasticity of the PDMS may alter the cavitation dynamics compared to a rigid target [20,23], no unique process or perforation of the material was observed during or post experiments. Due to fast bubble collapse and expansion during the exposure period of 10 µs, there exist instances where the bubble walls appear blurry or where the bubble and plasma can be seen in the same image as seen in Figure 4a, $t = 100\ \mu s$ and in Figure 4b, $t = 0\ \mu s$ respectively. The bubble reaches a maximum diameter

at 50 μs, and collapses at 100 μs after which the bubble splits into several micro-bubbles. As seen in the images, some of these micro-bubbles condensate rapidly and others remain in the site 1 ms after the cavitation event.

Figures 4b-4d show the cavitation dynamics above the β_{100}, β_{125}, and β_{150} samples; respectively. In general, the experiments performed with the microstructured surfaces show similar distinctions from the untreated case. First, at $t = 50\ \mu s$, the bubbles are notably deformed elliptically with a major axis parallel to the surface compared to a more spherical shape formed above the untreated sample. The microstructure surface appears to lift towards the bubble which is evidence of the expansion of entrapped air pockets that form when the microstructures are submerged in the water. At the maximum cavitation size ($t = 50\ \mu s$), the internal bubble pressure is equal to the saturation vapor pressure which is smaller than the surrounding hydrostatic pressure in the medium. This difference in pressure acts as a tensile force causing the entrapped air pockets to expand which in turn compress the cavitation bubble to an asymmetrical shape. The expanded entrapped air pockets are largest directly underneath the cavitation event and decrease radially outward. This radial dependence is more apparent at the time of bubble collapse (labeled on Figure 4c, $t = 100\ \mu s$) where the expanded air pockets form a cusp-like shape. The entrapped air pockets appear to have a delayed response to the cavitation collapse as compression of the internal bubble contents increase the local pressure which should cause the entrapped air pockets to contract.

Another contrast between the effects of the microstructures and that of the untreated sample is the increase of remnant gasses after the cavitation collapse. When collapsing

towards a solid boundary, the bubble impacts the surface and forms a vortex ring stretching radially outward, thus remaining gases stay near the surface [72]. In the case of the micro-structured samples, the air pockets contact the bubble and the liquid gap previously separating the bubble wall from the air pockets disappears. This suggests that some degree of coalescing occurs between the cavitation bubble and air pockets and likely among the air pockets themselves. The intense interaction during collapse between the two bulk gasses creates a cloud of bubbles in the vicinity, a portion of which is assumed to be mostly from the cavitation bubble which slowly migrates away from the surface. The remaining cloud of bubbles partially retracts towards the microstructure surface but ultimately does not resume to its initial state prior to the cavitation event. As seen in Figures 4b-4d, 1 ms after the cavitation event, the region above the microstructures has an increase in amount of visible air that has detached from each sample which gives way for the boxed crevices to be "deactivated" and filled with water to reach a wetted state. In the next section, the rates of crevice deactivation are reported. Figure 4d labels the detached air pockets and the repelled cavitation cloud mass.

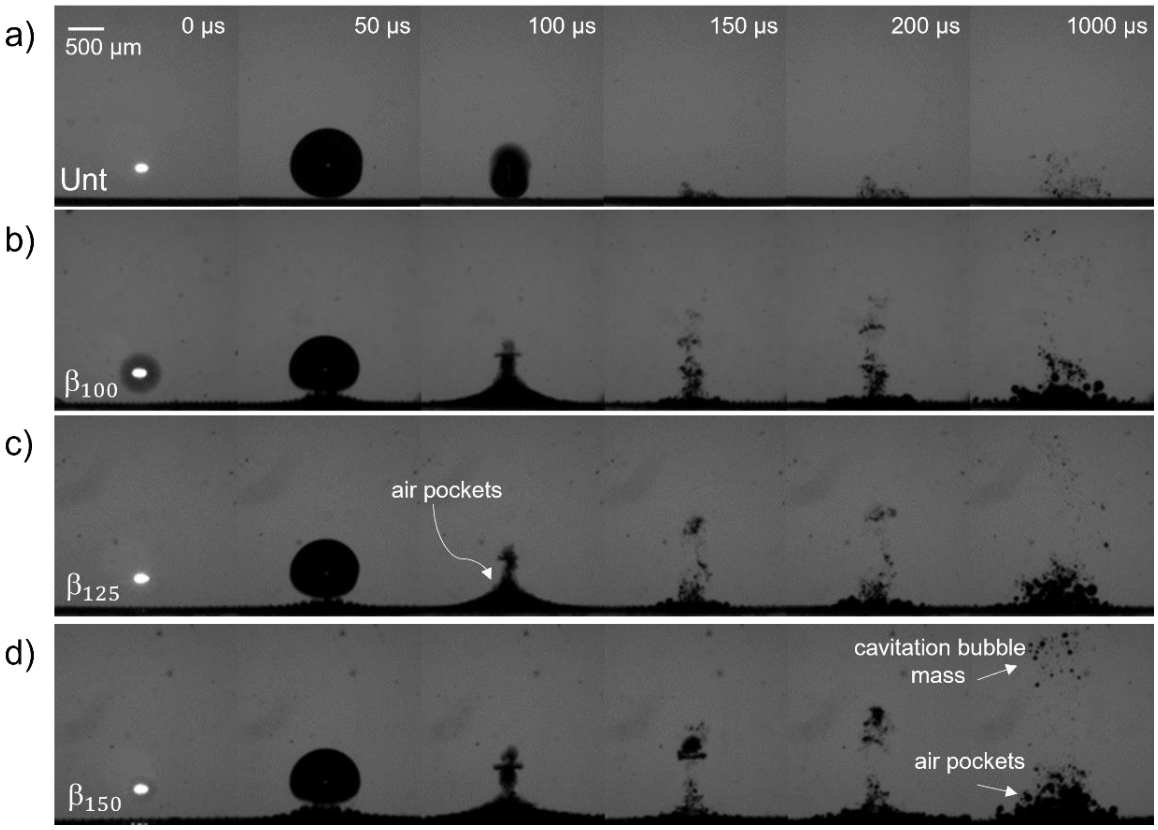

Figure 3-4: Comparison of a single cavitation bubble collapsing at a stand-off distance of γ = 1 from a) untreated PDMS, b) β_{100}, c) β_{125}, and d) β_{150} microstructures. The black line at the bottom of each image corresponds to the sample surface.

Figure 5 shows the representative cavitation dynamics above each sample at a further stand-off distance of γ = 2 where the distance between the cavitation bubble and the surfaces is increased by one radial unit, R_{max}. Once again, in the untreated sample, the cavitation bubble collapses toward the surface, but requires more time to reach impact. As such, the cavitation rebound can be seen in Figure 5a, at $t = 150\ \mu s$ where the bubble regrows to a new maximum with the remaining energy that was not dissipated [73]. At 200 μs, the bubble oscillates to a minimum again and continues approaching the sample. The

horizontal dotted white lines in Figure 5 are meant to show the position of zero displacement if the bubble collapsed without influence from surroundings. In the cases with the microstructured surfaces, the bubble is repelled as it was in the experiments with $\gamma = 1$, but the bubble retains a mostly spherical shape. The bulge from the protruding air pockets is hardly seen for β_{100} and β_{125} but is most noticeable for β_{150}. For $\gamma = 2$, at $t = 100\ \mu s$ the gasses only extend approximately 175 μm from the surface compared to roughly 370 μm for $\gamma = 1$ (difficult to distinguish due to coalescing) at the same time from bubble initiation. However, the EAPs still expand past the microstructure walls. Immediately after the first bubble collapse, the entrapped air pockets retract back flush with the surfaces as noted in the following frame (150 μs). It is important to highlight a new feature; when looking closely, one can see an elongated jet tip emerging from the rebound bubbles at $t = 150\ \mu s$ for all microstructures (see white arrows in Figures 5b-5d). The thin jet is less visible for the β_{125} sample which may simply be due to variation in time that the jet tip detaches from the bulk bubble. When the jet detaches, the small volume of gas condenses quickly as it is not observed in the subsequent frames. After 1 ms, detached EAPs are observed just above the surfaces with an apparent correlation to an increase in structure sizes (larger micro-crevices form larger area occupied by EAPs). However, as will be explained in the following section, the cross section of the wetted region (region with fully escaped air pockets), appears much smaller than at $\gamma = 1$ whose wetted region is on the order of the projected maximum bubble size. This decrease in wetting region can be attributed to the distant collapse of the cavitation bubble which produces a smaller driving pressure for the entrapped air pockets to grow from the surface.

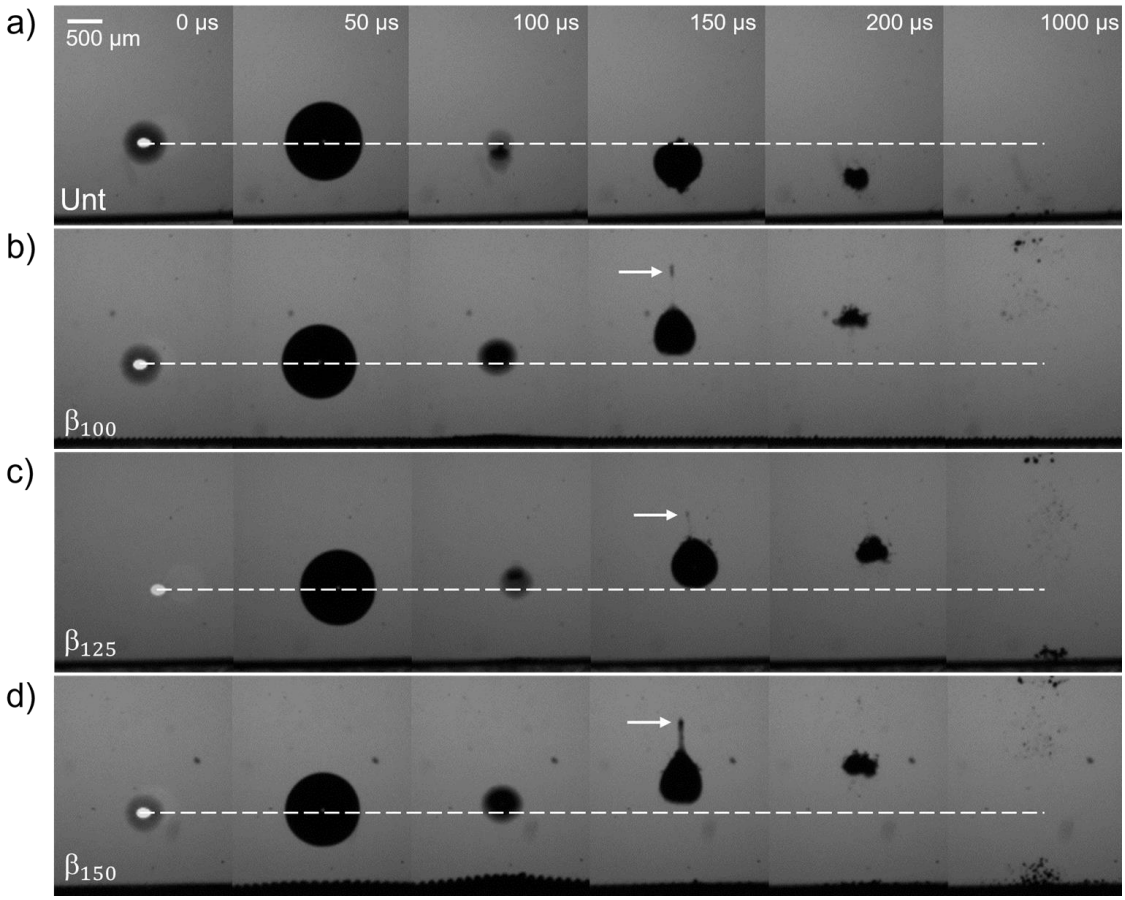

Figure 3-5: Comparison of a single cavitation bubble collapsing at a stand-off distance of γ = 2 from a) untreated PDMS, b) β_{100}, c) β_{125}, and d) β_{150} microstructures. The black line at the bottom of each image is the surface.

The micro-jet formation and evolution is shown with more temporal resolution in Figure 6 for the event from Figure 5b (γ = 2, β_{100}). The start of bubble migration away from the surface begins within 10 µs from the time of bubble collapse. During the collapse, the bubble emits a shockwave whose velocity decreases from a supersonic state to a sonic speed of ~1500 m/s within a few microns. The pressure wave propagates radially outward in all directions and reaches the expanded EAPs, where a significant portion is reflected

due to an acoustic impedance mismatch between DI water and the air [74,75]. It takes approximately 1.5 µs for the pressure wave to travel the total distance, to the EAPs and back to the bubble center (2 mm). The resulting present pressure waves contributes to the sum of forces (Kelvin Impulse) between the attractive Bjerness force towards the sample surface and the bouyancy forces acting on the bubble [76]. The reflected wave, interacts with the bubble wall, causing the lower surface to become a reentrant jet which exists the opposite wall with an average velocity of ~18 m/s (based on tracking the jet tip over 40 µs period). At the initial point of plasma formation and expansion, a first bubble-induced shockwave is formed, but jet formation prior to $t = 100\,\mu s$ is noted. This could be explained by the fact that the EAPs have not yet expanded, thus the pressure wave impacting the surface, interacts with a smaller gaseous volume along with making contact with the PDMS microstructure walls which absorb most of the acoustic energy as opposed to reflect it.

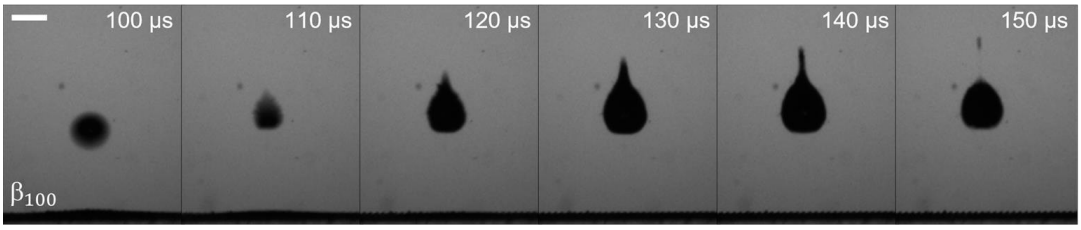

Figure 3-6: Sequence of images showing micro-jet evolution during cavitation bubble collapse ($\gamma = 2$, β_{100}). The scale bar is 500 µm.

Figure 7 shows the cavitation dynamics when the bubble is formed at $\gamma = 3$ from the surfaces. The general trend of the bubble migration remains as described for Figure 5, except with some missing features. First, no significant difference is noted at the surfaces

during the bubble lifetime. That is, with the present spatial and temporal resolution, the EAPs do not appear to expand. Secondly, the surface also appears to continue undisturbed 1 ms after the bubble generation which suggests that the microstructures have retained the entrapped air pockets and more cycles can be initiated with similar results. The micro-jet described in Figure 6, is still present but in a less defined form, appearing to break the top bubble wall in a broader area. Videos of representative dynamics shown in Figures in 4, 5 and 7 can be seen in Supplemental Video 1.

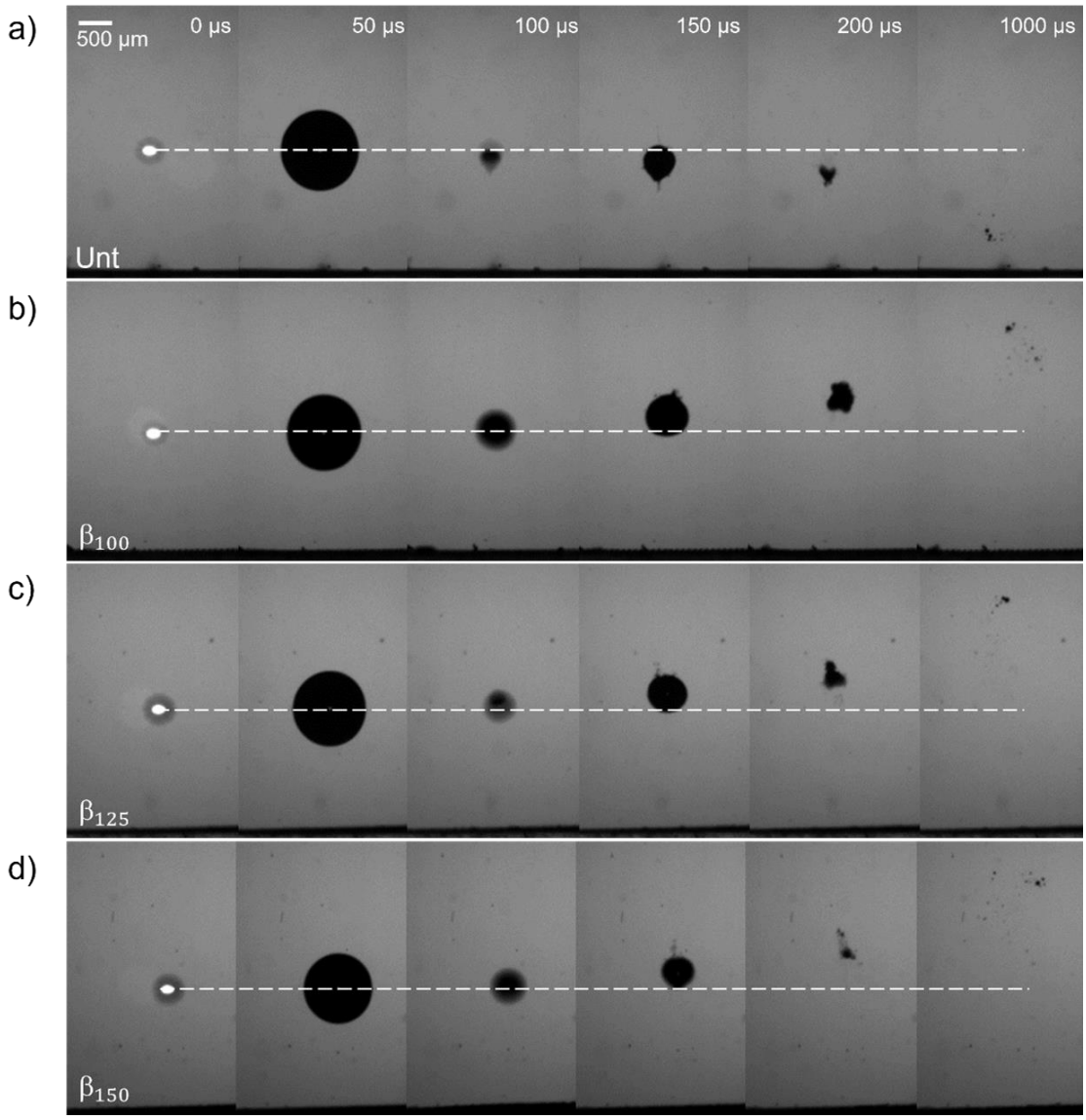

Figure 3-7: Comparison of a single cavitation bubble collapsing at a stand-off distance of γ = 3 from a) untreated PDMS, b) β_{100}, c) β_{125}, and d) β_{150} microstructures. The black line at the bottom of each image is the surface.

To directly compare the degree of repulsion or attraction depending on the surface, we processed the image stacks in ImageJ to track the bulk bubble centroid and determine the displacement over a period of 2 ms. The tracking of the bubble volume only considers

the y-direction from the point of bubble collapse which acts as the origin in time and space. As labeled in Figure 4d, the cavitation bubble rarely maintains a single volume, rather it tends to split to a bubble cloud of smaller, uncondensed vapor. By employing the minimum method during the binarization, the least dense and smallest bubble clouds were eliminated from the measurements. Figure 8 shows the displacement of the bubble volume where a positive value denotes repulsion from the surface and a negative value signifies attraction towards the surface. First, Figure 8a shows the displacement for each sample at a stand-off distance of $\gamma = 1$. The untreated case is not plotted due to the short stand-off distance and the bubble having already reached the surface at collapse (time 0 μs). The displacement of the cavitation bubble due to the three variable microstructures overlaps with minor differences. In Figures 8b and 8c, the displacements for $\gamma = 2$ and $\gamma = 3$ are shown with inclusion of the untreated case. It is important to note that in Figure 8b, the displacement values of the untreated case are stopped at a time shorter than 2 ms because the bubble volume has approached the surface and could no longer be accurately tracked in ImageJ due to difficulty in distinguishing the bubble volume from the blurry surface (caused by slight mis-levels with respect to the camera sensor). This issue arises for both Figure 8b and 8c which should reflect a displacement equal to the full distance of the bubble center to the surface as defined by the stand-off distance ($D_{\gamma=2}$ = ~1100 μm and $D_{\gamma=3}$ = ~1650 μm).

The displacements of β_{100} and β_{125} appear to continue overlapping while β_{150} begins to consistently show slightly larger displacements although not significant. This agrees with the observations from Figure 5 in that the larger EAP volumes can expand

further due to their larger individual volumes. However, by a direct comparison across γ = 2 and γ = 3, the further stand-off distance (Fig. 8c) causes a slower rate of bubble repulsion which is expected as the cavitation site is removed from the influence of the EAPs. Additionally, the repulsive displacements in Figure 8b and 8c appear symmetrical to the respective attraction towards the untreated surface which means the presence of the EAPs can be described as an imaginary smooth flat boundary above the cavitation bubble opposite of the true surface.

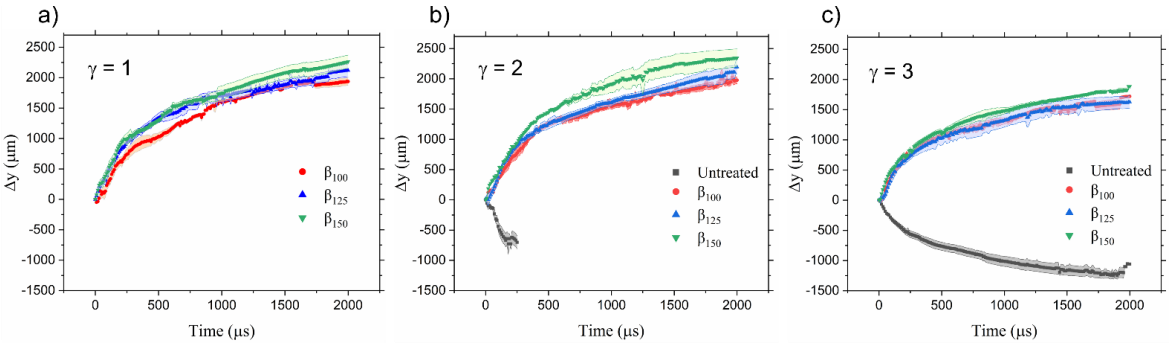

Figure 3-8: Average displacement of cavitation bulk volume following collapse near microstructure samples and an untreated PDMS at a) γ = 1, b) γ = 2, and c) γ = 3. Displacements shown correspond to a single cavitation event formed above pristine samples. Time 0 μs depicts moment of cavitation bubble collapse. Positive displacement is migration away from surface.

3.3.2. Subsequent cavitation events and wetting of microstructures

The observed behaviors described in the previous section are limited by the structures' ability to hold the entrapped air stable after a cavitation cycle. To quantify the stability and robustness of the samples to withstand multiple cavitation events, we formed a series of 50 subsequent cavitation bubbles atop each structure at a frequency of 0.066 Hz. This frequency was chosen as it is the lowest driving frequency of the pulsed laser which maximizes the time between bubbles (15 seconds) to create as close to a static initial condition as possible which would allow for the EAPs and water interface to settle for clearer top-view images. The camera in Figure 3 labeled "CCD", captured a top view of the boxed crevices after each cavitation event, approximately 100 ms prior the following bubble. To quantify the wetting behavior of the microstructures, we introduce a dimensionless parameter, wetted region. The wetted region W_r, is defined by equation 1):

$$W_r = \frac{N_{wetted} * A_\beta}{A_C} \quad (1)$$

where N_{wetted} is the number of completely deactivated crevices (no partial wetting is counted), A_β is the surface area of a single square crevice and A_C is the projected area of an average cavitation bubble. Figure 9 shows the wetting progression of the structures after 50 cavitation events in 5 event increments. Three regions are seen in Figure 9a which correspond to γ = 1, 2 and 3 are highlighted in blue, yellow, and pink respectively. For the largest stand-off distance of 3, the wetted region remains relatively constant for all microstructures, only reaching $W_r = 0.17$, 0.23 and 0.27 for β_{100}, β_{125}, and β_{150} respectively after 50 cavitation cycles for which the three surfaces still repelled the bubbles.

In comparison, Avila et al. reported stable entrapped air and cavitation repulsion from their silica-GEMS for up to 30 cycles for $3 < \gamma < 5.1$ [62]. More clear distinctions between the microstructures are seen for $\gamma = 2$ where the largest wetted regions exist for β_{150} and the lowest for β_{100}. This occurs because as seen by the hydrophobic properties from Figure 2, β_{100} microstructures are most robust against transition from a Cassie-Baxter state to a Wenzel state. At this distance, the β_{100} microstructures incur a wetted region of $W_r = 3.1$ after 50 cavitation cycles, a wetted region that is reached by the β_{125} and β_{150} samples after only ~25 and ~15 events respectively. At a stand-off distance of 1, the cavitation bubble clearly coalesces with the EAPs (as described earlier in section 3.1) thus the wetted regions are much larger than the projected bubble area, exceeding $W_r > 4$ event after only 1 cavitation event for all microstructured samples.

Figure 9b shows representative images across the three stand-off distances (β_{125}) post 50 cavitation events. As seen in the image of $\gamma = 3$, the wetted crevices are not in a well-defined central region compared to the closer stand-off distances. These randomized positions may be attributed to slight variations in the quality of the PDMS casted walls as opposed to the cavitation dynamics themselves. Some of the crevices are partially wetted, but retained a small fraction of the EAP, typically adhered to one of the four corners.

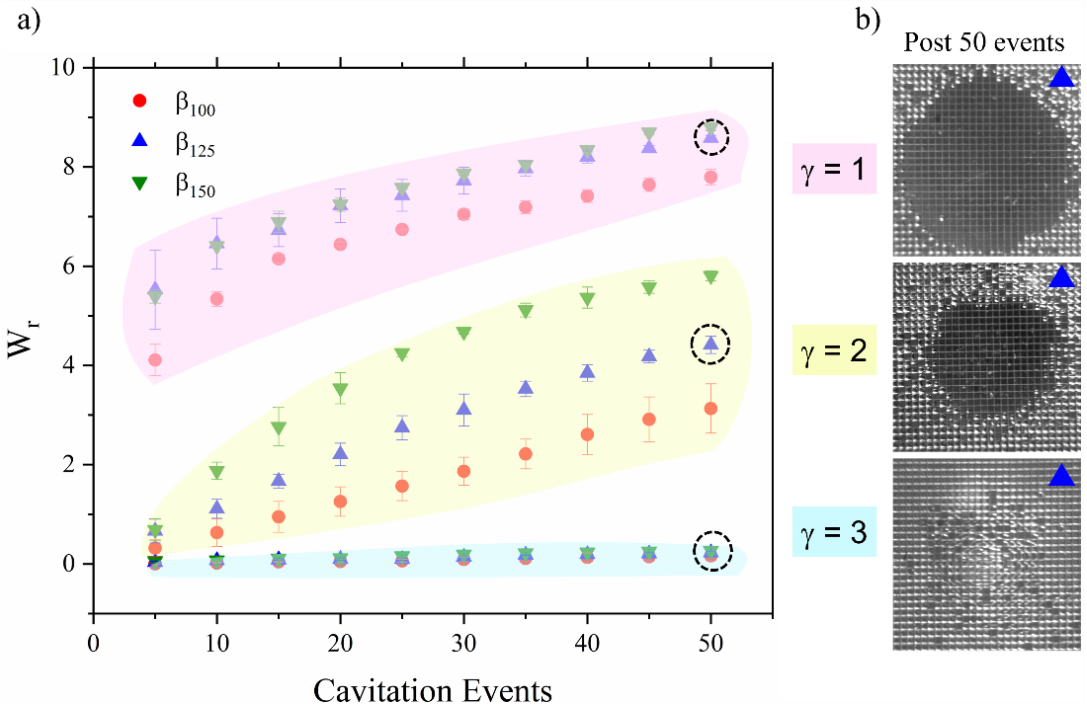

Figure 3-9: a) Average wetted region of each microstructure sample following a sequence of cavitation events. Data points are highlighted to show their corresponding stand-off distances (pink, yellow and blue for γ = 1, γ = 2, and γ = 3 respectively) b) Representative top view (CCD camera) of β_{125} microstructures after 50 cavitation events for each stand-off distance. The length of the blue triangle shown in the images is 500 µm.

A mid stand-off distance ($\gamma = 2$) was chosen for a direct comparison of the wetting behavior after 25 and 50 events for each sample. Figure 10 shows the reference with an overlay of the average bubble diameter for reference. The smallest structure size (β_{100}) is most robust even after 50 cavitation cycles, matching a similar wetted region as β_{125} after only half the events. As the crevices release the compressible EAPs, they begin to resemble an untreated-like surface. Figure 10b shows the displacement of a cavitation bubble after 1, 25 and 50 cavitation cycles. After 25 cavitation events, the migration of the bubble is

decreased drastically to an average displacement of 1 mm with a velocity of ~0.3 m/s compared to the average velocity of the first bubble of 1 m/s. Eventually, the surface behaves as a flat, smooth boundary and a reversal in migration of the bubble occurs. After 50 events, the cavitation bubble appears to no longer be influenced by the remaining EAPS and the displacement approaches a mirror shape of the first event.

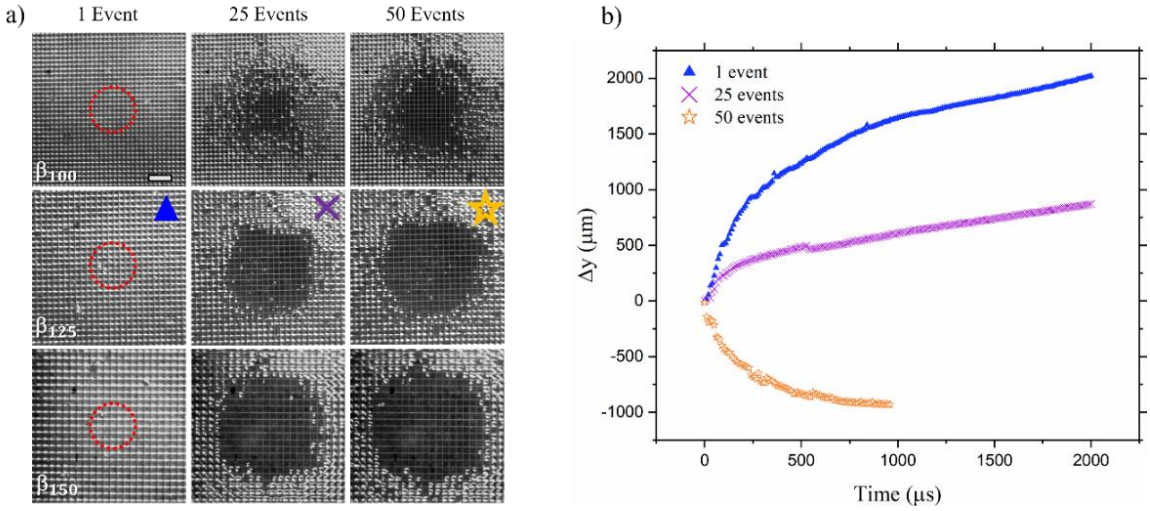

Figure 3-10: a) Top view of microstructures showing wetting progression. Red dashed circle represents the projection of the maximum bubble size. Scale bar is 500 μm. b) Displacement of cavitation bubble after 1, 25 and 50 events.

3.3.3. Particle Tracking Visualization

As seen in Figures 4-7, the bubble displacement can be quantified by tracking the bubble volume which is visible due to the miss match in refractive index between the gas and water. However, the shadowgraphy images do not provide information on the surrounding response to the cavitation events. Thus, to visualize the surrounding flows we embedded tracer particles in the water and recorded a series of 10 cavitation events ($\gamma = 2$) atop an untreated surface and a β_{125} sample at a frame rate of 250 fps within an 8.5 x 8.5 mm^2 FOV. The first column of Figure 11a shows the binarized reference prior to the first cavitation event. The white pixels correspond to the fluorescing microspheres, and the orange circle represents the size and location of the cavitation bubbles above the tested PDMS sample (black rectangular region). The red dashed frame shows the FOV used in the shadowgraph experiments (Figures 4-7). The frame rate was reduced to enlarge the FOV and to increase the exposure time, a requirement to observe the low intensity fluorescence. The second column shows the sum of image stacks across the 10 cavitation events which creates streak lines that the particles formed. While the streak lines do not capture the full trajectory of a particle due to various particles entering and leaving the light sheet (and the camera's focal plane), they offer a short snapshot of the surrounding flow. As seen in the streak image of the flow above the untreated surface, a vortex is formed expanding in an approximate area of 2 x 2 mm^2 which was not possible to observe in the shadowgraph images of the same conditions (Figure 5). The streak image of the microstructure case (bottom row) shows paths extending from the center of the sample surface as well as new particles entering the FOV from the right and left boundaries. When

compared to the untreated case, more streak lines exist above the microstructured surface suggesting higher degrees of agitation and displacement of fluid. The downward migration of the cavitation bubble towards the untreated surface is restricted by the surface itself, absorbing the fluids' kinetic energy which may lead to surface damage under certain conditions and specific materials [65]. In contrast, the cavitation events produced in proximity to the microstructured surface are repelled upwards (including the 10th event per Figure 10b), without physical barriers which gives way for more fluid flow. While some of the motion is due to bubble clusters from the cavitation remnant gases and detached EAPs, the fluorescence nature of the microspheres and binarization removes their contribution in the track measurements.

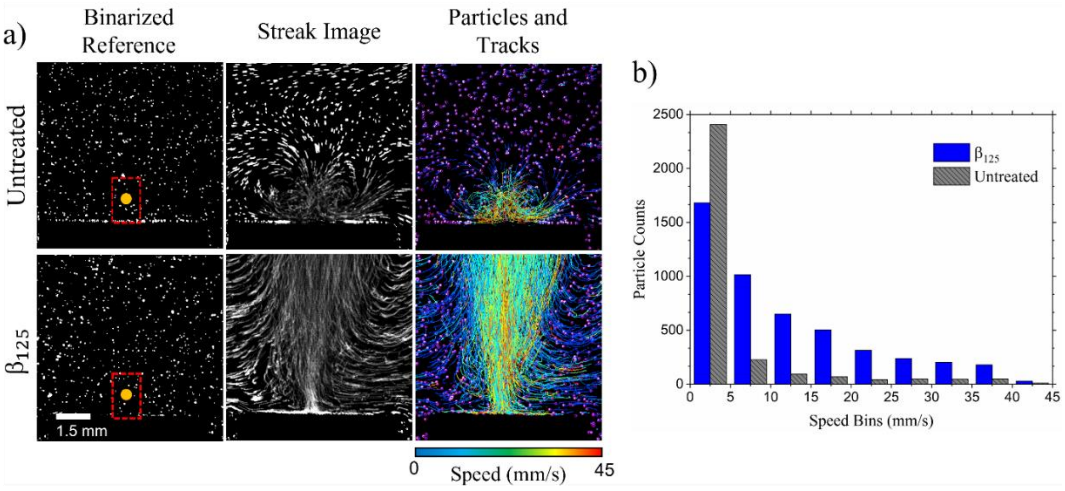

Figure 3-11: a) Pathlines of seeded fluorescent particles to show dynamics following cavitation bubble collapses near b) an untreated PDMS surface and b) a β_{125} microstructure surface.

The particles were tracked over time using the Track Mate plugin [77,78] in ImageJ which overlays the track displacements as seen in the third column of Figure 11a. The

particles are outlined in purple, and the tracks are color coded based on the maximum speed at any point during the tracking. As noted in both the untreated and microstructured case, the highest speeds appear in the center of the image, in line where the cavitation bubbles are formed, and the track speeds decrease radially outward from the centerline. Supplemental Video 2 shows the full dynamics of Figure 11a. Figure 11b shows the distribution of the track speeds in bin ranges of 5 mm/s increments. It is evident that the EAPs increase the count of particles in the FOV that experience disturbance, a 60% increase in displaced particles across all speeds.

3.4. Conclusion

In this study, we analyzed the interaction between laser-induced cavitation bubbles and entrapped air pockets in hydrophobic microstructures. The microstructures were fabricated using a simple laser ablation method that can create reusable molds and easily scaled to different dimensions. Several experiments were conducted over three stand-off distances to quantify the degree of repulsion and stability of the surfaces. In all cases near the untreated surface, the bubble collapses towards the boundary, producing a radially expanding toroidal impact on the surface. In contrast, the microstructured surfaces tend to repel the cavitation bubble while there are sufficient in-tact EAPs. The stability of the entrapped airs is directly dependent on the surfaces' hydrophobicity and number of incident cavitation cycles. Smaller microstructures, hence smaller, but equally dense entrapped air pockets, consistently result in smaller wetted regions. Over time, however the surfaces become deactivated and enter a wetted Wenzel state where they begin to resemble the dynamics of a flat untreated surface. By

employing a technique to stabilize the entrapped air pockets, this interaction may be a viable solution to decrease cavitation erosion or magnify flows in microfluidic applications.

Additional Information

Supplementary Information The online version contains supplementary material available online

Correspondence and requests for materials should be addressed to G. A.

Reprints and permissions information is available at www.nature.com/reprints.

Acknowledgements

V. Robles was supported by the Ford Foundation Predoctoral Fellowship. JC. Gonzalez-Parra acknowledges support from UC-MEXUS CONACYT (Fellowship number 825115). The authors are grateful to Dr. David G. Carter and the Microscopy and Imaging Core Facility for SEM training and usage. Additionally, the authors thank Dr. Masaru P. Rao for discussion related to the fabrication of the microstructures.

Author Statement

V. R.: Conceptualization, Formal analysis, Methodology, Investigation, Writing - original draft, Writing – review & editing, Visualization. **J. C. G. P.:** Investigation, Writing – review. **N. C. E.:** Conceptualization, Methodology, Writing - original draft, Writing – review & editing, Visualization, Supervision. **G. A.:** Conceptualization, Supervision.

Declaration of Competing Interest

The authors declare that they have no competing financial or personal interests that could influence this work.

Chapter 4. Future Studies

Each of the works described in Chapters 2 and 3 uncovered additional fundamental areas of cavitation to explore as well as potential applications of the detailed dynamics. The following sections will highlight future studies that may be carried out to further understand, control and predict the outcomes of each work. Additionally, the final section of this chapter provides a summary of the work conducted on thermocavitation (another form of optical cavitation) and possible avenues to expand this work.

4.1. Double Bubble Jetting – Future Work

As described in Chapter 2, a system of two interacting cavitation bubbles can form fast, focused microjets. Two lasers, with similar optical parameters (energy and wavelength) were used to form equally sized bubbles to reduce the variable parameters to spatial and temporal separation of the bubbles. While the use of two individual lasers provides more control of the bubbles' relative temporal and spatial formations, two lasers increase the cost operations of the systems and create an initial time investment to optimize their synchronizations. The two-bubble micro jetting configuration may be simplified with the use of one laser divided into two paths using a beam splitter. Doing so, will result in simultaneous laser induced optical breakdown at the sites where the beams are focused which would correlate to a bubble-bubble temporal separation of $\tau = 0$. At this time delay, two similarly sized bubbles will attract each other. However, by varying the ratio of incident energies (e.g. 70/30 beam splitter), the collapse time of one bubble relative to the second can be increased or decreased. As was explained in section 2.4, two processes must

occur for an optimal jet formation: 1) the elongation of a bubble is required, and 2) the elongated tip must be reversed by surrounding pressures accelerating the asymmetrical inflow. However, these physical processes are not likely to occur with cavitation events formed at the same time. While a temporal delay is possible with the use of a fiber cable, or a continuous wave laser with a mechanical beam chopper, the bubbles' growth and collapse rates can be varied simply by their relative energies and thus, resulting sizes. This type of interaction requires further investigation and redefining of the inter-bubble stand-off distance nondimensional number (γ_{BB}). The interaction of different sized cavitation bubbles formed at the same time has been previously studied by L. W. Chew et al.[25] and J. Luo et al. [79]. However, Chew and Luo's works conducted experiments using electric discharge which creates an intrusive process through wires. Additionally, they reported different cases of bubble-bubble separation which could lead to coalescence, jetting towards or jetting away. This topic could be further investigated with the use of laser cavitation.

Varying fluid properties than also can affect the bubble sizes and thus jet formation and velocity. For instance, at smaller scales surface tension will play a larger role in the conical reversal. At smaller bubble radii, the internal pressures will be larger which may increase the rate of jet travel. Other factors such as surrounding boundaries (i.e. air interfaces, solid walls) may also affect the formation or jet velocities. In the study presented in this work, the bubble-target stand-off distance was varied but the effect on the jet velocity was assumed to be negligible. In the presence of a nearby boundary, the bubbles will grow elliptically and be prematurely attracted or repelled from each other. Such

influence can be utilized to optimize jet formation in the case of minimal to no temporal inter-bubble delay. Characterization of these mentioned properties and conditions is required to effectively control the jetting process.

After jet formation, the transition through the cavitating liquid and through additional fluids is also critical to understand for the advancement towards needle-free alternatives. For instance, the micro jet is surrounded by a vapor "blanket" which quickly recondenses into water. By using PIV or PTV, the jet flow in the immediate vicinity can be visualized and the length and velocity of the jet can be more accurately measured. Thus, the degree that jet impact and shear forces contribute to damage on soft materials can be identified. With such information, certain parameters may be controlled to keep the surrounding vapor blanket more stable and reduce the shear on the jet, reducing the damping. The jet transition into different media can also be further explored.

First, the jet impact into tissue surrogate agar was explored, but there remain unanswered questions. For instance, if the surrounding vapor fails to recondense into liquid, then air bubbles will form and be entrapped in the solid medium. This can pose clogging issues in the material which is typically a negative effect to be avoided in biological systems. Apart from clogging issues, the existing microbubbles can be nucleation points for other cavitation events to form under the influence of subsequent DBJ events. Such process may lead to severe internal damage within the material to inject. To study the internal stresses due to these potential internal cavitation events, laser speckle imaging (LSI) may be implemented. LSI can be used through transmission or reflection of a continuous wave laser on a diffusive medium such as agar with dispersed particles. The

implementation of LSI can provide a map of static and dynamic regions during the cavitation impact by performing a statistical analysis on a stack of images. For instance, Figure 4-1**Error! Reference source not found.** shows preliminary LSI images of cavitation formed inside of 1% agar. A 543 nm HeNe laser with 0.5 mW of power was used as the probe laser. The three images show an average of ten frames over 200 µs after calculation of the contrast, K_t, which is defined by the normalized standard deviation of each pixel. The formation and propagation of dynamic zones are suggested by the color map which shows radial dependence from the bubble axis and dynamic regions even 400 µs after bubble collapse. This approach requires further optimization and improvement of the analysis by further decreasing the camera exposure time, increasing the temporal resolution and using back-scattering imaging.

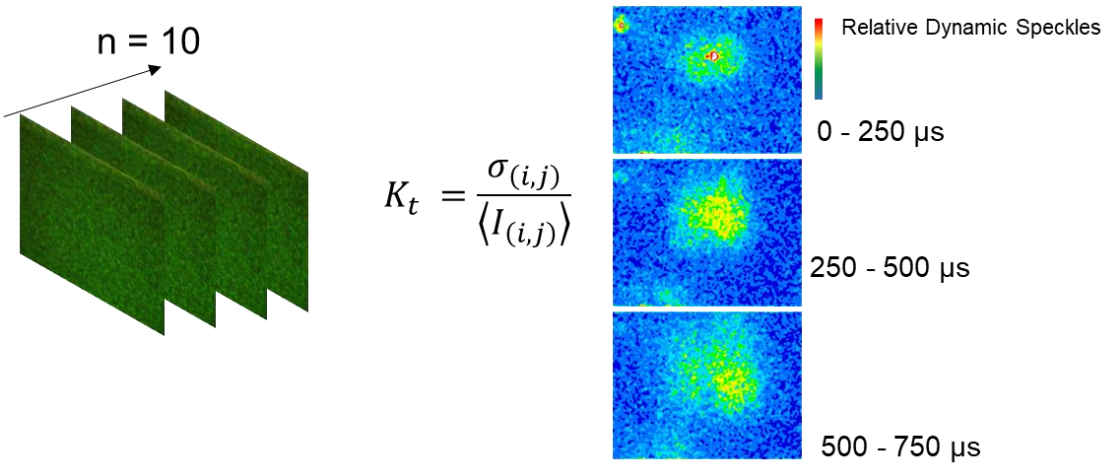

Figure 4-1: LSI analysis of cavitation induced inside 1% agar.

4.2. Gas Entrapping Microstructures - Future Work

The proposed mechanism of cavitation bubble repulsion from the hydrophobic PDMS gas-entrapping surfaces is the reflection of a pressure wave which creates a pressure imbalance. This hypothesis was assumed using an estimation of the shockwave decay and travel speed through the water. However, by implementing a hydrophone, the true shockwave travel speed can be determined. Several representative positions can be chosen to obtain pressure measurements with the use of a hydrophone (PVDF/fiber optic) at high temporal resolution. By observing the rise in signal over the relative positions of the hydrophone from the PDMS structures, the rate and magnitude of pressure wave travel can be correlated to high-speed frames and matched with the moment of jet reversal.

Another area of interest to explore is the potential applications of the dynamics that occur with the interaction of a cavitation bubble with the gas-entrapping microstructures. First, as seen in section 0, there is an increase in agitation to the surrounding. This enhanced agitation, compared to a bubble collapsing near an untreated surface may be used for mixing in microfluidic scales where laminar flows are most present. This method of using cavitation and gas entrapping structures may serve as an on-demand, active agitator compared to permanently built structures or mixers. To observe these effects, a parametric study can be performed followed by an experimental analysis. For instance, Figure 2-2 shows a preliminary Ansys simulation of a y-shape microchannel with two inlets and one outlet. By inserting two different fluids (different densities) into the inlets, a laminar flow can be formed with a steady state condition. However, with the introduction of a cavitation bubble in the center of the channel, the bubble growth and collapse can generate a

homogeneous mixture of the two fluids. Further experimentation and simulations are needed to estimate the time to reestablish a laminar flow after a single cavitation bubble. Additionally, the gas-entrapping microstructures could be embedded in the microchannel walls to observe if the additional agitation is sustained for enhanced mixing.

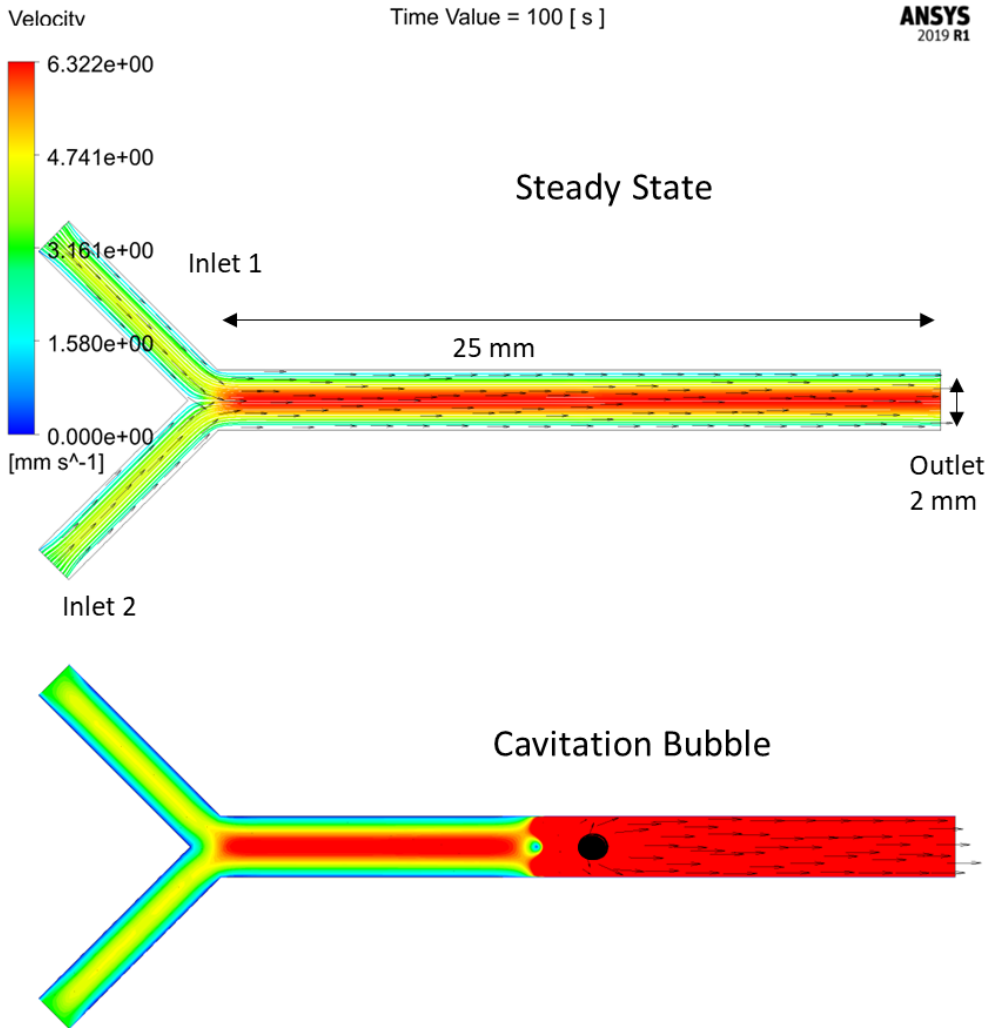

Figure 4-2: Ansys simulation showing effects of cavitation bubble induced in y-shaped microchannel.

Another potential application of the resulting dynamics of a cavitation bubble interacting with gas-entrapping microstructures is utilizing the agitation as an on-demand heat transfer enhancer. Under sentient conditions, the air pockets can provide a slip condition for a flowing fluid. Thus, a reduction in driving pressure may be observed at the cost of a lower rate of heat transfer due to the insulating property of air (lower heat transfer coefficient). However, upon activating the expansion of the air pockets, any developed thermal boundary layer can be destroyed, and fresh coolant can contact the heated microchannel walls. Thus, further experiments can be conducted to maximize the hydraulic performance index ratio which is defined by the ratio of the Nusselt number, and the pressure drops normalized by the values of a flat smooth surface. Finally, different geometries and scales could be explored to further maximize and stabilize the air entrapment over larger number of incident cavitation events. A proposed mechanism to prolong the life of air entrapment would be to incorporate laser-induced periodic surface structures (LIPSS), a nano-scale roughness as described by J.C. Gonzalez-Parra [65].

4.3. Thermocavitation –Summary & Future Work

Optical cavitation occurs when a laser superheats an absorptive liquid and creates a vapor bubble. When the vapor bubble collapses, energy is emitted in the form of an acoustic shockwave. Optical cavitation includes two types: thermocavitation and ionocavitation. The distinction comes from the method in which the liquid is heated. Optical thermocavitation, as opposed to ionocavitation, is described by a process where the laser directly superheats the liquid to a critical temperature beyond its boiling point. Continuous wave (CW) lasers produce this as opposed to pulsed wave lasers which carry high energy density per pulse. With the use of CW lasers (thermocavitation), a strongly absorbing liquid is superheated and explosively driven to vaporization[80]. A bubble grows and collapses giving way to increased temperatures, pressures and emission of a compressive wave. Due to short light penetration into the absorptive liquid, thermocavitation always occurs hemispherical in nature and attached to a substrate. Thermocavitation occurs quasi-periodically reaching diameters, lifetimes and frequencies up to 2 mm, 1 ms and 5 kHz with higher powers and absorption producing higher frequencies, smaller bubbles, lower pressure waves, and faster nucleation[37,81,82]. Table 2 summarizes the differences in the cavitation dynamics.

Rastopov and Sukhodolsky induced optical thermocavitation with continuous wave (CW) lasers in the 1990s to study fluid composition [1, 2]. The use of low-power CW lasers for inducing cavitation has paved the way for many applications because of their simplicity and low cost. 20 years after Rastopov and Sukhodolsky observed CW cavitation, Ramirez-San-Juan, et al produced cavitation using a CW laser focused into a saturated solution of

copper nitrate [3]. Their research investigated the relationship between cavitation frequency and laser power. Increasing laser power correlates to an increase in the frequency of cavitation events.

Table 2: Formation of optical cavitation via pulsed and continuous wave lasers

	PULSED: "LASER-INDUCED CAVITATION"	CONTINUOUS WAVE: "THERMOCAVITATION"
DESCRIPTION	High laser energy density, transparent medium	Strongly absorbing liquid
HEATING	Instantaneous breakdown	Duration of heating prior to bubble nucleation is dependent on power density and absorptivity. O(100 ms),
BUBBLE	Laser pulse ionizes liquid. Plasma vaporizes surrounding liquid and emits shockwave. (~1mm, ~ 20-150μs)	Parcel of fluid at focal point is superheated to spinodal limit and vaporized, emitting a pressure wave. Bubble is hemispherical (~2mm, ~1ms)
GROWTH	High-temperature, high-pressure vapor rapidly expands until saturation pressure is reached and temporary equilibrium occurs with condensation and evaporation through bubble wall.	
COLLAPSE	Surrounding pressure dominates internal saturation pressure and accelerates bubble walls towards implosion. As bubble volume decreases, internal pressures and temperatures rise again and second pressure wave is emitted.	
REBOUND	Bubble regrows and oscillates until energy dissipates. Satellite bubbles may appear from nearby dissolved gasses.	

The thermal responses of surrounding fluid and surfaces which is typically ignored or avoided, but if optimized, may enhance heat transfer. Electronic components continue to rapidly miniaturize and increase power consumption, leading to amplified thermal management issues from 1) high heat fluxes (approaching 10^5 W/cm^2), 2) confined space constraints, and 3) non-uniform localized to hotspots. Conventional systems inevitably fail to address these issues due to their large form factors, required mechanically moving parts, or failure to reach confined hotspots. Thermocavitation may serve as an on-demand localized agitator with a smaller cost basis than ionocavitation.

Several fundamental studies conducted in Dr. Aguilar's lab sought to characterize the optical and fluid effects on thermocavitation dynamics such as size, frequency formation and time. More application-based experimentation would greatly enforce the findings reported in these previous works. For example, planar laser induced fluorescence (PLIF) was utilized as a non-intrusive temperature field measurement around a thermocavitation bubble. Figure 4-3 shows the temperature measurement leading up to, during and following the collapse of a single bubble. As noted, a thermal boundary layer builds up during the irradiation of the laser until a bubble is nucleated and collapses, dissipating the energy and cooling the site of bubble formation before the boundary layer is rebuilt.

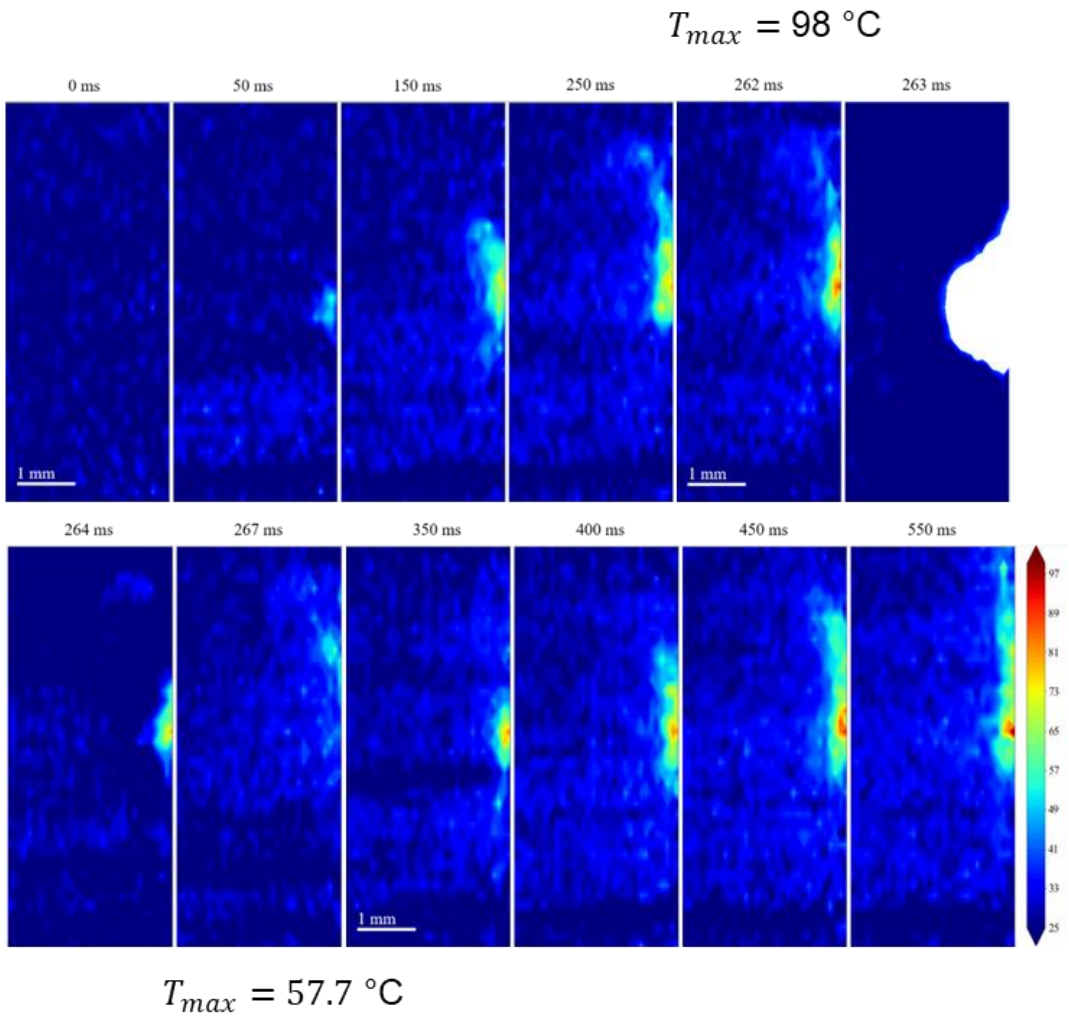

Figure 4-3: Temperature measurements during the bubble's growth, near its maximum diameter, and during its collapse. The time listed above each image represent the amount of time that has passed since the activation of the pump laser. The scale on the right is temperature in °C.

While this was observed experimentally, further experimentation with an externally heated wall can show the efficiency of using thermocavitation for cooling. A computational simulation may provide information on how to optimize bubble size, and position to ensure high rates of heat transfer with minimal damage potentials. Figure 4-4 shows a preliminary

set of simulations completed in COMSOL which show the reduction in accumulated heat with a constant jet impingement of 10 Hz. This frequency was chosen to match the typical operating rate of a pulsed laser but using thermocavitation may provide higher rates of bubble formation and collapse up to 100 Hz as observed by B. Zhang et al. [82]. The conducted simulations can be paired with experimental work by fabricating a microchannel using PDMS casting of a 3D printed mold. Using PDMS is beneficial in that it is a transparent medium in which Rhodamine-B may be embedded prior to curing for a fluorescent-based temperature measurement. A non-intrusive temperature measurement is ideal as infrared cameras are costly and other methods such as the use of point thermocouples can interfere with the cavitation dynamics. Additionally, the corrosive nature of copper nitrate makes it an unfavorable cavitation fluid to use. Thus, other colloidal solutions of nanoparticles or absorbing natural dyes should be investigated such as was reported by S. Afanador-Delgado et al. [83,84.]

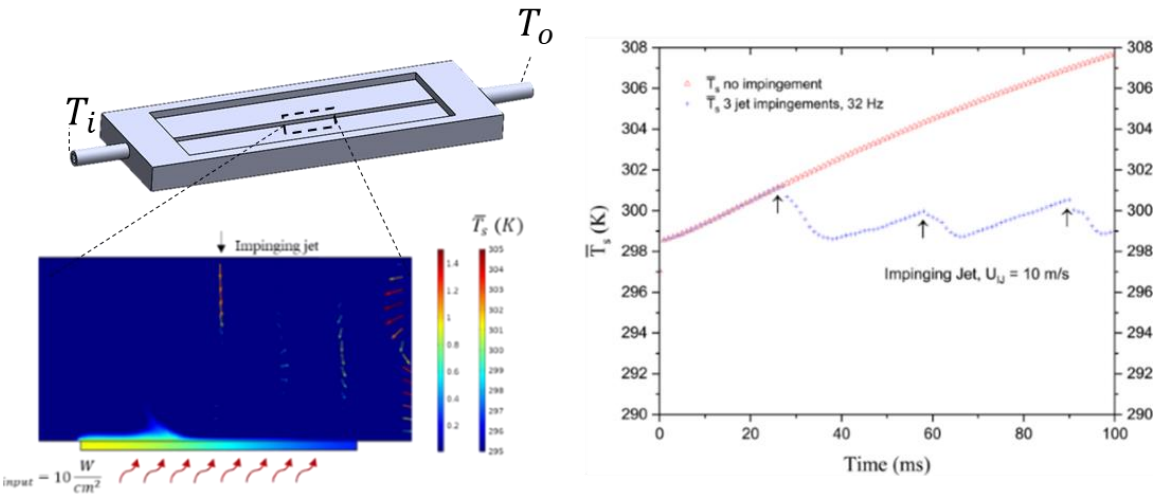

Figure 4-4: COMSOL simulation showing straight microchannel with 1 inlet and 1 outlet. The simulation shows an externally heated wall impacted by an impinging jet. The plot shows the wall temperature over time with and without an imping jet.

Chapter 5. Conclusion

Cavitation studies stemmed from observing surface damage on nautical equipment where cavitation leads to material breakdown, vibrations and erosion overtime due to strong emitted shockwaves and microjets. Recent studies exploit cavitation for particle fragmentation, microfluidic controls and a multitude of biomedical techniques, however, cavitation damage mechanisms remain important and not fully understood. In this described work, the cavitation impacts are observed, analyzed and effectively controlled from the perspective of safe employment of targeting soft materials and repelling cavitation from a surface.

Cavitation has been the source of negative damage on various materials, but with the ability to efficiently tune emerging microjets and distancing the point source of intense plasmas and shockwaves, it can prove powerful for emerging application such as soft material perforation and enhanced heat transfer. By consolidating this work, comprehensive understanding of governing factors on microjet formation and insight into mechanisms of damage has been investigated.

References

[1] F. Reuter and R. Mettin, Ultrasonics Sonochemistry **29**, 550 (2016).
[2] C.D. Ohl, M. Arora, R. Dijkink, V. Janve, and D. Lohse, Applied Physics Letters **89**, (2006).
[3] B. Verhaagen and D. Fernández Rivas, Ultrasonics Sonochemistry **29**, 619 (2016).
[4] R. Dijkink, S. Le Gac, E. Nijhuis, A. Van Den Berg, I. Vermes, A. Poot, and C.D. Ohl, Physics in Medicine and Biology **53**, 375 (2008).
[5] Y. Arita, M. Ploschner, M. Antkowiak, F. Gunn-Moore, and K. Dholakia, Optics Letters **38**, 3402 (2013).
[6] C. Wei, J. Xia, M. Lombardo, C. Perez, B. Arnal, K. Larson-Smith, I. Pelivanov, T. Matula, L. Pozzo, and M. O'Donnell, Optics Letters **39**, 2599 (2014).
[7] S.D. George, S. Chidangil, and D. Mathur, Langmuir **35**, 10139 (2019).
[8] N. Zamora-Romero, V. Robles, C. Alvarez, N. Cuando-Espitia, L.F. Devia-Cruz, E. Penilla, D.L. Halaney, and G. Aguilar, Optics InfoBase Conference Papers **Part F61-E**, 1041707 (2017).
[9] D. Banks, V. Robles, B. Zhang, L.F. Devia-Cruz, S. Camacho-Lopez, and G. Aguilar, Experimental Thermal and Fluid Science **103**, 385 (2019).
[10] B. Liu, J. Cai, and X. Huai, International Journal of Heat and Mass Transfer **78**, 830 (2014).
[11] W. Lauterborn and H. Bolle, Journal of Fluid Mechanics **72**, 391 (1975).
[12] E.A. Brujan, G.S. Keen, A. Vogel, and J.R. Blake, Physics of Fluids **14**, 85 (2002).
[13] G.Y. Yuan, B.Y. Ni, Q.G. Wu, Y.Z. Xue, and A.M. Zhang, Journal of Fluids and Structures **92**, (2020).
[14] L. Van Wijngaarden, Ultrasonics Sonochemistry **29**, 524 (2016).
[15] P.A. Barnes and K.E. Rieckhoff, Applied Physics Letters **13**, 282 (1968).
[16] A. Vogeland and W. Lauterborn, Journal of the Acoustical Society of America **84**, 719 (1988).
[17] R. Timm, Journal of Fluid Mechanics **206**, 299 (1989).
[18] C. Lechner, W. Lauterborn, M. Koch, and R. Mettin, Physical Review Fluids **4**, (2019).
[19] E.A. Brujan, K. Nahen, P. Schmidt, and A. Vogel, Journal of Fluid Mechanics **433**, 251 (2001).
[20] E.A. Brujan, K. Nahen, P. Schmidt, and A. Vogel, Journal of Fluid Mechanics **433**, 283 (2001).
[21] D. Horvat, U. Orthaber, J. Schille, L. Hartwig, U. Löschner, A. Vrečko, and R. Petkovšek, International Journal of Multiphase Flow **100**, 119 (2018).
[22] A. Vogel and V. Venugopalan, Chemical Reviews **103**, 577 (2003).
[23] W. Xu, Y. Zhai, J. Luo, Q. Zhang, and J. Li, Experimental Thermal and Fluid Science **109**, 109897 (2019).
[24] B. Han, K. Köhler, K. Jungnickel, R. Mettin, W. Lauterborn, and A. Vogel, Journal of Fluid Mechanics **771**, 706 (2015).
[25] L.W. Chew, E. Klaseboer, S.W. Ohl, and B.C. Khoo, Physical Review E - Statistical, Nonlinear, and Soft Matter Physics **84**, (2011).

[26] C.T. Hsiao, J.K. Choi, S. Singh, G.L. Chahine, T.A. Hay, Y.A. Ilinskii, E.A. Zabolotskaya, M.F. Hamilton, G. Sankin, F. Yuan, and P. Zhong, Journal of Fluid Mechanics **716**, 137 (2013).
[27] J.C. Stachowiak, T.H. Li, A. Arora, S. Mitragotri, and D.A. Fletcher, Journal of Controlled Release **135**, 104 (2009).
[28] J. Baxter and S. Mitragotri, Journal of Controlled Release **106**, 361 (2005).
[29] V. Menezes, S. Kumar, and K. Takayama, Journal of Applied Physics **106**, 1 (2009).
[30] C. Berrospe-Rodriguez, C.W. Visser, S. Schlautmann, D.F. Rivas, and R. Ramos-Garcia, Journal of Biomedical Optics **22**, 1 (2017).
[31] Y. Tagawa, N. Oudalov, C.W. Visser, I.R. Peters, D. van der Meer, C. Sun, A. Prosperetti, and D. Lohse, Physical Review X **2**, 1 (2012).
[32] T.H. Han and J.J. Yoh, Journal of Applied Physics **107**, 1 (2010).
[33] N. Kyriazis, P. Koukouvinis, and M. Gavaises, Proceedings of the Royal Society A: Mathematical, Physical and Engineering Sciences **475**, (2019).
[34] M. Moradiafrapoli and J.O. Marston, Chemical Engineering Research and Design **117**, 110 (2017).
[35] L. Oyarte Gálvez, M. Brió Pérez, and D. Fernández Rivas, Journal of Applied Physics **125**, 14 (2019).
[36] R. Zaca-Morán, J. Castillo-Mixcóatl, N.E. Sierra-González, J.M. Pérez-Corte, P. Zaca-Morán, J.C. Ramírez-San-Juan, R. Ramos-García, and J.P. Padilla-Martínez, Optics Express **28**, 4928 (2020).
[37] J.P. Padilla-Martinez, C. Berrospe-Rodriguez, G. Aguilar, J.C. Ramirez-San-Juan, and R. Ramos-Garcia, Physics of Fluids **26**, (2014).
[38] S.F. Rastopov and A.T. Sukhodolsky, in *USSR Academy of Sciences* (1990), pp. 127–134.
[39] H. Jang, E. Hur, Y. Kim, S.-H. Lee, N.G. Kang, and J.J. Yoh, Journal of Biomedical Optics **19**, 118002 (2014).
[40] P.A. Quinto-Su, M. Suzuki, and C.D. Ohl, Scientific Reports **4**, 1 (2014).
[41] Z. Han, J. Li, M. Singh, C. Wu, C.H. Liu, S. Wang, R. Idugboe, R. Raghunathan, N. Sudheendran, S.R. Aglyamov, M.D. Twa, and K. V. Larin, Physics in Medicine and Biology **60**, 3531 (2015).
[42] X. Liang, IEEE Trans Biomed Eng. **57**, 953 (2013).
[43] I. Akhatov, O. Lindau, A. Topolnikov, R. Mettin, N. Vakhitova, and W. Lauterborn, Physics of Fluids **13**, 2805 (2001).
[44] P.K. Kennedy, D.X. Hammer, and B.A. Rockwell, Progress in Quantum Electronics **21**, 155 (1997).
[45] G.H. Goldsztein, Studies in Applied Mathematics **112**, 101 (2004).
[46] J. Schramm and S. Mitragotri, Pharmaceutical Research **19**, 1673 (2002).
[47] K. Cu, R. Bansal, S. Mitragotri, and D. Fernandez Rivas, Annals of Biomedical Engineering (2019).
[48] E.L. Giudice and J.D. Campbell, Advanced Drug Delivery Reviews **58**, 68 (2006).
[49] H. Jang, E. Hur, Y. Kim, S.-H. Lee, N.G. Kang, and J.J. Yoh, Journal of Biomedical Optics **19**, 118002 (2014).

[50] M. Ahearne, Y. Yang, A.J. El Haj, K.Y. Then, and K.K. Liu, Journal of the Royal Society Interface **2**, 455 (2005).
[51] E.A. Brujan, T. Noda, A. Ishigami, T. Ogasawara, and H. Takahira, Journal of Fluid Mechanics **841**, 28 (2018).
[52] Y. Zhang, X. Qiu, X. Zhang, and N. Tang, Ultrasonics Sonochemistry **67**, 105157 (2020).
[53] J. Cui, Z.P. Chen, Q. Wang, T.R. Zhou, and C. Corbett, Ultrasonics Sonochemistry **64**, 104951 (2020).
[54] T. Trummler, S.H. Bryngelson, K. Schmidmayer, S.J. Schmidt, T. Colonius, and N.A. Adams, Journal of Fluid Mechanics **899**, (2020).
[55] L. Duchemin, S. Popinet, C. Josserand, and S. Zaleski, Physics of Fluids **14**, 3000 (2002).
[56] J.P. Padilla-Martinez, J.C. Ramirez-San-Juan, N. Korneev, N. Banks, G. Aguilar, and R. Ramos-Garcia, Atomization and Sprays **23**, 517 (2013).
[57] V. Robles, E. Gutierrez-Herrera, L.F. Devia-Cruz, D. Banks, S. Camacho-Lopez, and G. Aguilar, Physics of Fluids **32**, 042005 (2020).
[58] A.N. Hellman, K.R. Rau, H.H. Yoon, S. Bae, J.F. Palmer, K.S. Phillips, N.L. Allbritton, and V. Venugopalan, Analytical Chemistry **79**, 4484 (2007).
[59] B. Hayes, A. Hayes, M. Rolleston, A. Ferreira, and J. Krisher, ASME International Mechanical Engineering Congress and Exposition, Proceedings (IMECE) **7**, 1 (2018).
[60] R. Dijkink and C.D. Ohl, Lab on a Chip **8**, 1676 (2008).
[61] D. Banks, V. Robles, B. Zhang, L.F. Devia-Cruz, S. Camacho-Lopez, and G. Aguilar, Experimental Thermal and Fluid Science **103**, 385 (2019).
[62] S.R. Gonzalez-Avila, D.M. Nguyen, S. Arunachalam, E.M. Domingues, H. Mishra, and C.D. Ohl, Science Advances **6**, 1 (2020).
[63] M. Dular, T. Požar, J. Zevnik, and R. Petkovšek, Wear **418–419**, 13 (2019).
[64] H.J. Sagar, S. Hanke, M. Underberg, C. Feng, O. el Moctar, and S.A. Kaiser, Materials Performance and Characterization **7**, 20180038 (2018).
[65] J.C. Gonzalez-Parra, V. Robles, L.F. Devia-Cruz, R.I. Rodriguez-Beltran, N. Cuando-Espitia, S. Camacho-Lopez, and G. Aguilar, Surfaces and Interfaces **29**, (2022).
[66] X. Yang, C. Liu, D. Wan, and C. Hu, Physics of Fluids **33**, 73311 (2021).
[67] B.M. Borkent, S. Gekle, A. Prosperetti, and D. Lohse, Physics of Fluids **21**, 1 (2009).
[68] H.J. Kwon, J. Yeo, J.E. Jang, C.P. Grigoropoulos, and J.H. Yoo, Materials **11**, (2018).
[69] J. Liu, B. Li, T. Zhu, Y. Zhou, S. Li, S. Guo, and T. Li, Biomicrofluidics **13**, 034114 (2019).
[70] I. Miranda, A. Souza, P. Sousa, J. Ribeiro, E.M.S. Castanheira, R. Lima, and G. Minas, Journal of Functional Biomaterials **13**, (2022).
[71] R. Das, Z. Ahmad, J. Nauruzbayeva, and H. Mishra, Scientific Reports 2020 10:1 **10**, 1 (2020).
[72] F. Reuter, S.R. Gonzalez-Avila, R. Mettin, and C.D. Ohl, Physical Review Fluids **2**, 1 (2017).
[73] R. Hicking and M.S. Plesset, Physics of Fluids **7**, 7 (1964).
[74] J.P. Padilla-Martinez, J.C. Ramirez-San-Juan, C. Berrospe-Rodriguez, N. Korneev, G. Aguilar, P. Zaca-Moran, and R. Ramos-Garcia, Applied Optics **56**, 7167 (2017).

[75] P. Koukouvinis, M. Gavaises, O. Supponen, and M. Farhat, Physics of Fluids **28**, (2016).
[76] J.R. Blake, D.M. Leppinen, and Q. Wang, Interface Focus **5**, 1 (2015).
[77] D. Ershov, M.-S. Phan, J.W. Pylvänäinen, S.U. Rigaud, L. le Blanc, A. Charles-Orszag, J.R.W. Conway, R.F. Laine, N.H. Roy, D. Bonazzi, G. Duménil, G. Jacquemet, and J.-Y. Tinevez, BioRxiv 2021.09.03.458852 (2021).
[78] J.Y. Tinevez, N. Perry, J. Schindelin, G.M. Hoopes, G.D. Reynolds, E. Laplantine, S.Y. Bednarek, S.L. Shorte, and K.W. Eliceiri, Methods **115**, 80 (2017).
[79] J. Luo and Z. Niu, Scientific Reports **9**, 1 (2019).
[80] J.C. Ramirez-San-Juan, E. Rodriguez-Aboytes, A.E. Martinez-Canton, O. Baldovino-Pantaleon, A. Robledo-Martinez, N. Korneev, and R. Ramos-Garcia, Optics Express **18**, 8735 (2010).
[81] J.C. Ramirez-San-Juan, J.P. Padilla-Martinez, P. Zaca-Moran, and R. Ramos-Garcia, Optical Materials Express **1**, 598 (2011).
[82] B. Zhang, D. Banks, V. Robles, L.F. Devia Cruz, and G. Aguilar, Experimental Thermal and Fluid Science **136**, 110683 (2022).
[83] S.M. Afanador-Delgado, R. Sevilla-Escoboza, V.F. Marañón-Ruíz, and R. Chiu, Optics and Laser Technology **132**, (2020).
[84] S.M. Afanador-Delgado, R. Sevilla-Escoboza, V.F. Marañón-Ruíz, and R. Chiu, Optics and Laser Technology **132**, 106468 (2020).